



L 98-59: A Benchmark System of Small Planets for Future Atmospheric Characterization

Daria Pidhorodetska¹ , Sarah E. Moran² , Edward W. Schwieterman^{1,3,4,5} , Thomas Barclay^{6,7} , Thomas J. Fauchez^{6,8,9} ,
Nikole K. Lewis¹⁰ , Elisa V. Quintana⁶ , Geronimo L. Villanueva⁶ , Shawn D. Domagal-Goldman^{4,6} ,
Joshua E. Schlieder⁶ , Emily A. Gilbert^{6,7,9,11,12} , Stephen R. Kane¹ , and Veselin B. Kostov^{6,9,13}

¹ Department of Earth and Planetary Sciences, University of California, Riverside, CA, USA

² Department of Earth and Planetary Sciences, Johns Hopkins University, 3400 North Charles Street, Baltimore, MD 21218, USA

³ NASA Astrobiology Alternative Earths Team, Riverside, CA, USA

⁴ Nexus for Exoplanet System Science (NExSS) Virtual Planetary Laboratory, Seattle, WA, USA

⁵ Blue Marble Space Institute of Science, Seattle, WA, USA

⁶ NASA Goddard Space Flight Center, 8800 Greenbelt Road, Greenbelt, MD 20771, USA

⁷ University of Maryland, Baltimore County, 1000 Hilltop Circle, Baltimore, MD 21250, USA

⁸ Goddard Earth Sciences Technology and Research (GESTAR), Universities Space Research Association (USRA), Columbia, MD, USA

⁹ GSFC Sellers Exoplanet Environments Collaboration, Greenbelt, MD, USA

¹⁰ Department of Astronomy and Carl Sagan Institute, Cornell University, 122 Sciences Drive, Ithaca, NY 14853, USA

¹¹ Department of Astronomy and Astrophysics, University of Chicago, 5640 South Ellis Avenue, Chicago, IL 60637, USA

¹² The Adler Planetarium, 1300 South Lake Shore Drive, Chicago, IL 60605, USA

¹³ SETI Institute, 189 Bernardo Avenue, Suite 200, Mountain View, CA 94043, USA

Received 2021 January 26; revised 2021 June 29; accepted 2021 July 1; published 2021 September 29

Abstract

The M3V dwarf star L 98-59 hosts three small ($R < 1.6 R_{\oplus}$) planets. The host star is bright ($K = 7.1$) and nearby (10.6 pc), making the system a prime target for follow-up characterization with the Hubble Space Telescope (HST) and the upcoming James Webb Space Telescope (JWST). Herein, we use simulated transmission spectroscopy to evaluate the detectability of spectral features with HST and JWST assuming diverse atmospheric scenarios (e.g., atmospheres dominated by H_2 , H_2O , CO_2 , or O_2). We find that H_2O and CH_4 present in a low mean molecular weight atmosphere could be detected with HST in one transit for the two outermost planets, while H_2O in a clear steam atmosphere could be detected in six transits or fewer with HST for all three planets. We predict that observations using JWST/NIRISS would be capable of detecting a clear steam atmosphere in one transit for each planet and H_2O absorption in a hazy steam atmosphere in two transits or less. In a clear, desiccated atmosphere, O_2 absorption may be detectable for all three planets with NIRISS. If the L 98-59 planets possess a clear, Venus-like atmosphere, NIRSpec could detect CO_2 within 26 transits for each planet, but the presence of H_2SO_4 clouds would significantly suppress CO_2 absorption. The L 98-59 system is an excellent laboratory for comparative planetary studies of transiting multiplanet systems, and observations of the system via HST and JWST would present a unique opportunity to test the accuracy of the models presented in this study.

Unified Astronomy Thesaurus concepts: Exoplanet atmospheres (487); Transmission spectroscopy (2133); Low mass stars (2050); Extrasolar rocky planets (511); Exoplanets (498); Near infrared astronomy (1093); Astronomy data modeling (1859)

1. Introduction

Thousands of planets orbiting stars outside of our solar system have been confirmed, the vast majority of which were detected with the transit method. The Kepler and K2 missions (Borucki et al. 2010; Howell et al. 2014) taught us that planets and their host stars are remarkably diverse (e.g., Borucki et al. 2011; Lissauer et al. 2011; Batalha 2014; Bryson et al. 2020; Gaudi et al. 2020), and that planets are likely more abundant than stars in our galaxy (Burke et al. 2015; Dressing & Charbonneau 2015). While Kepler provided an unprecedented bounty of planets that enabled exoplanet population statistics, relatively few planets discovered by Kepler make ideal follow-up targets due to their large average distances. However, recent discoveries by ground-based telescopes of more readily characterizable Earth-sized worlds, such as the seven TRAPPIST-1 planets (Gillon et al. 2016, 2017), are enabling us to learn about the properties of rocky planets beyond our solar

system. The Transiting Exoplanet Survey Satellite (TESS; Ricker et al. 2015), launched in 2018, is currently performing a near-all-sky survey to search for planets orbiting bright stars in our solar neighborhood. Planets that orbit bright stars are favorable targets for probing bulk compositions and atmospheres, particularly those orbiting M dwarfs, because of the large planet-to-star radius ratio and favorable transit probabilities for close-in planets. As TESS reveals new exoplanets, the prospect of discovering new worlds and probing their atmospheres provides an exciting opportunity to broaden our understanding of the nature of planets that may resemble our own.

Despite having a shorter observing baseline than Kepler, TESS has begun to uncover several multiplanet systems. Transiting multiplanet systems provide controlled environments for comparative planetary studies, as planets that form around the same star—and thus come from the same nebula and protoplanetary disk—share many properties that are typically less well constrained when comparing planets in different systems. Such shared properties include the host star’s mass, composition, activity level, formation history, and evolution. Multiple planet systems in resonant chains also

strongly increase the exchange of torque at each planet conjunction, offering a unique opportunity to characterize the physical properties through transit timing variations (TTVs; Agol et al. 2005; Holman & Murray 2005). However, the vast majority of known multiplanet systems (transiting or otherwise) orbit stars that are too distant and faint for atmospheric characterization studies with the Hubble Space Telescope (HST) or the upcoming James Webb Space Telescope (JWST).

Small, potentially rocky planets that are suitable for such studies are particularly scarce. To date, very few planets whose densities may be consistent with a terrestrial composition have transmission spectroscopy measurements. These planets include those in the TRAPPIST-1 system (de Wit et al. 2016, 2018; Gillon et al. 2017; Luger et al. 2017; Delrez et al. 2018; Ducrot et al. 2018, 2020; Burdanov et al. 2019; Agol et al. 2021), as well as GJ 1132 b (Berta-Thompson et al. 2015; Southworth et al. 2017; Diamond-Lowe et al. 2018; Libby-Roberts et al. 2021; Mugnai et al. 2021), LHS 1140b (Dittmann et al. 2017; Diamond-Lowe et al. 2020a; Edwards et al. 2021) and LHS 3844b (Vanderspek et al. 2019; Kreidberg et al. 2019; Diamond-Lowe et al. 2020b). While no significant atmospheric detection has yet been made for any of these worlds, these observations have been highly informative. For example, HST observations of the TRAPPIST-1 planets have ruled out cloud/haze-free H₂-dominated atmospheres (de Wit et al. 2016, 2018; Wakeford et al. 2019a). Moran et al. (2018) explored whether hazy H₂-rich atmospheres could explain HST observations and found that laboratory measurements suggested that haze formation would be inefficient for hot H₂ atmospheres. De Wit et al. (2016, 2018), Moran et al. (2018), and Wakeford et al. (2019a) also determined that these planets' atmospheres may be composed of a wide variety of compositions dominated by higher molecular weight species such as N₂, O₂, H₂O, CO₂, or CH₄. As important as these results are, due to the limited sample size, it may be premature to draw general conclusions. Fortunately, TESS is eagerly anticipated to discover a few benchmark systems with nearby bright stars, large planet-to-star ratios, and close-in planets that will provide numerous transits that amplify their signal (Barclay et al. 2018).

Many of the planets that are the focus of follow-up observations, including atmospheric characterization, orbit M dwarfs. Such planets are important for constraining these observations, as low-mass stars account for the majority of stars in the galaxy (Henry et al. 2006; Winters et al. 2015). The M dwarfs range from about a tenth to half of a solar mass and are significantly less luminous than the Sun (luminosities range from one-twentieth of the Sun's luminosity from M0V stars to as low as several thousand times less luminous than the Sun for late M dwarfs) but display variable but most often higher activity levels (Kiraga & Stepien 2007; Hawley et al. 2014). The M dwarf stars undergo a prolonged, high-luminosity pre-main-sequence phase (Ramirez & Kaltenegger 2014; Luger & Barnes 2015; Tian & Ida 2015), where the total luminosity of the star can be as much as 2 orders of magnitude larger than the main-sequence luminosity. This has the potential to desiccate a planet by evaporating all/any water from the surface to the atmosphere, where strong UV radiation from the star can photodissociate water molecules into hydrogen and oxygen, creating the radicals H and OH (in some cases O). Hydrogen can escape to space, potentially leaving oxygen behind. This process would also catalyze the destruction and reprocessing of many gases in the atmosphere, reducing their overall lifetime

(e.g., CO + OH → CO₂ + H). In turn, M dwarf planets can retain their atmospheres from this phase through either outgassing of secondary atmospheres or surviving the pre-main-sequence phase due to large initial volatile endowments (Bolmont et al. 2017; Bourrier et al. 2017).

Multiplanet systems around M dwarf stars are common (e.g., Howard et al. 2012; Muirhead et al. 2015; Mulders et al. 2015; Hardegree-Ullman et al. 2019; Hsu et al. 2020). With numerous small planets in multiplanet systems, we can delve into questions about the origin and evolution of such small planets. Such queries can be solved with transmission photometry and spectroscopy—measuring the starlight filtered through the planet's atmosphere and observing the absorption at particular wavelengths to infer the presence of specific atoms and molecules. In making these measurements, we naturally must ask: what kind of atmospheres do these worlds have? Where did these atmospheres come from? Are they primordial and hydrogen-rich, as with comparatively well-characterized hot Jupiters, or are they secondary outgassed atmospheres primarily composed of heavier molecules, such as H₂O, CO₂, or even O₂? How do their atmospheric compositions vary depending on their current incident radiation? Do they contain clouds or hazes? Do rocky planets orbiting M dwarfs have atmospheres at all? A particularly intriguing planetary system orbits the nearby M dwarf L 98-59.

Three planets orbiting the nearby star L 98-59 were detected by the TESS transit detection pipeline (Jenkins et al. 2016), and their planetary nature was confirmed through supporting ground-based observations and statistical analyses (Kostov et al. 2019a). The M3V star L 98-59 has $M_* = 0.31 \pm 0.03 M_\odot$, $R_* = 0.31 \pm 0.01 R_\odot$, and $T_{\text{eff}} = 3412 \pm 49$ K (Cloutier et al. 2019). It is a main-sequence M dwarf and estimated to be >1 Gyr in age (Kostov et al. 2019b), inferred from the star's Hertzsprung–Russell diagram position, lack of spectroscopic youth indicators, slow rotation, no evidence of variability due to spots, and low levels of white-light flare activity as seen in TESS data. This quiescence indicates that the star is beyond the active youth phase characteristic of young M dwarfs. The lack of spot variability and infrequent flare rate is advantageous for conducting transit spectroscopy observations of the planets in this system.

At 10.6 pc, L 98-59 is the second-closest transiting multiplanet system to the Sun (after HD 219134). The planets have orbital periods of 2.25, 3.69, and 7.45 days, encompassing a near-resonant configuration. The masses of the outer two planets have been measured using ground-based radial velocity observations from HARPS (Cloutier et al. 2019), at $2.42 \pm 0.35 M_\oplus$ for L 98-59 c and $2.31 \pm 0.46 M_\oplus$ for L 98-59 d. Planet L 98-59 b is the smallest, innermost planet, and the current radial velocity measurements only allow for an upper limit of its mass at $<1.01 M_\oplus$ (at 95% confidence). These masses, combined with the radii of the three planets (0.80–1.57 R_\oplus), indicate that the two innermost planets have bulk densities that are almost certainly rocky (Dressing et al. 2015; Rogers 2015; Chen & Kipping 2016; Fulton et al. 2017; Owen & Wu 2017), while the outermost planet yields a bulk density that is consistent with substantial volatile content, suggesting that it is likely a mini-Neptune.

The L 98-59 planets receive significantly more energy than modern Earth receives from the Sun (a factor of 4–24 more than Earth's current irradiation), placing them in the Venus Zone (VZ; Kane et al. 2014), an annulus where the received

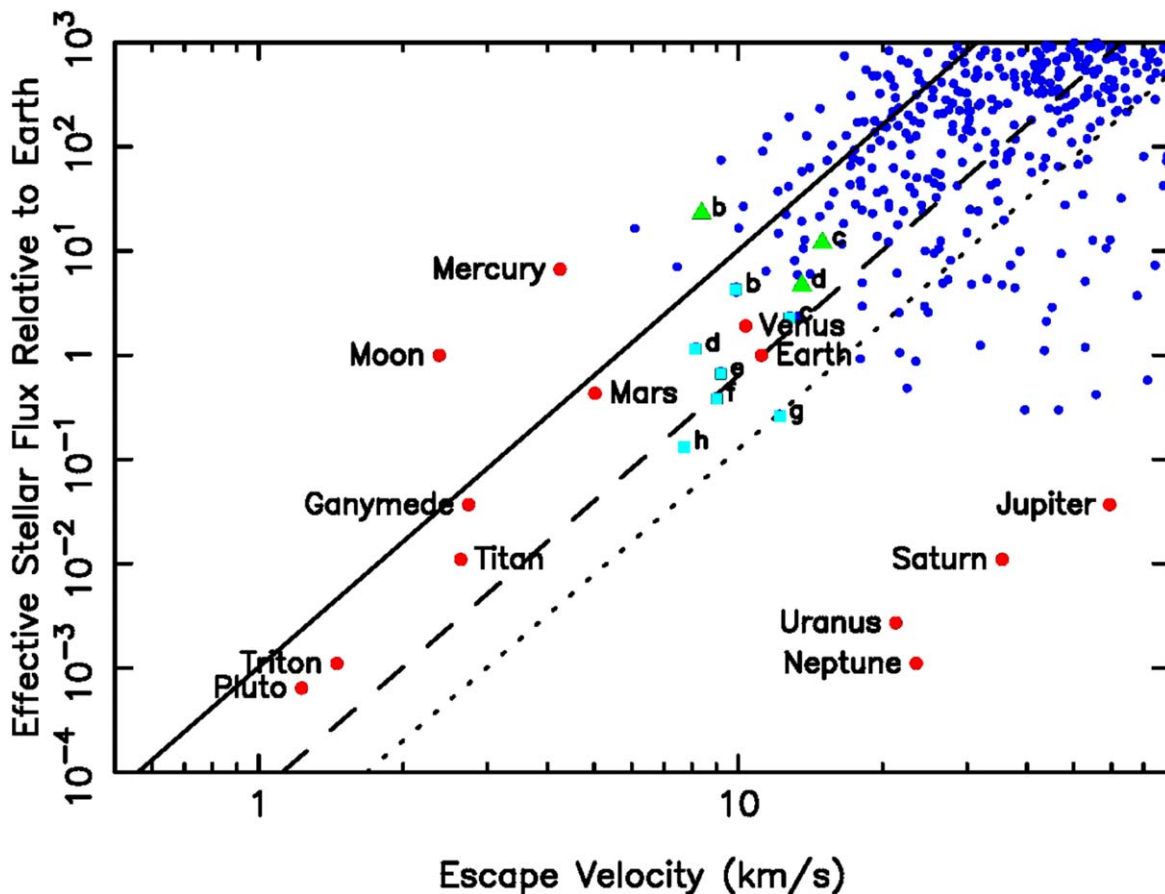


Figure 1. Representation of the cosmic shoreline (Zahnle & Catling 2017), shown as a solid line. Additional dashed and dotted lines assume XUV flux 16 and 256 times higher than solar, respectively. Solar system bodies are shown as red circles, and exoplanets are shown as blue dots. The L 98-59 and TRAPPIST-1 planets are indicated by green triangles and cyan squares, respectively.

flux of the planets would likely push a terrestrial planet like Earth into a runaway greenhouse state, producing conditions similar to those found on Venus while not completely stripping the atmosphere of volatiles or refractory elements, such as silicates. Studying planets that may be undergoing or have evolved into a post-runaway greenhouse state is valuable, as it can help teach us why some planets are Venus-like and others Earth-like (Ehrenreich et al. 2012). Although the post-runaway greenhouse state of Venus has rendered its atmosphere much different than that of Earth and ultimately uninhabitable, Venus and Earth share strong similarities in their size, density, and composition. Thus, studying Venus analogs allows us to place constraints on habitability, as atmospheric evolution of Venus-/Earth-sized planets points toward runaway greenhouse conditions (Kasting 1988; Leconte et al. 2013b; Kane et al. 2018). Although TESS is expected to discover ~ 300 Venus-analog planets (Ostberg & Kane 2019), most Venus-analog candidates discovered to date orbit relatively faint stars (Barclay et al. 2013; Kane et al. 2013, 2018; Angelo et al. 2017; Gillon et al. 2017). Fortunately, L 98-59 is bright ($K = 7.1$) and will therefore enable follow-up characterization of the planets' atmospheres, revealing which have Venus-like conditions. In that respect, L 98-59 could become a benchmark system.

Furthermore, the relative size and insolation fluxes of the L 98-59 planets places them within an interesting regime of potentially significant atmospheric loss. Shown in Figure 1 is a representation of the cosmic shoreline, which explores the

relationship between X-ray and ultraviolet (XUV) flux and the escape velocity for solar system objects with respect to atmospheric retention (Zahnle & Catling 2017). The solar system objects are marked as red circles, and the solid line is the cosmic shoreline, based on the empirically determined estimates of Zahnle & Catling (2017). Objects to the left of the solid line tend to lack atmospheres, whereas objects to the right do have atmospheres, albeit tenuous ones for those close to the line. We include two additional lines, dashed and dotted, that represent XUV factors 16 and 256 higher than solar, respectively (Roettenbacher & Kane 2017). We also include known exoplanets, shown as blue dots, for which the required data are available from the NASA Exoplanet Archive (Akeson et al. 2013). The location of the TRAPPIST-1 and L 98-59 planets are indicated by cyan squares and green triangles, respectively. Although the TRAPPIST-1 planets have a relatively high risk of significant atmospheric loss (Roettenbacher & Kane 2017; Cohen et al. 2018), the L 98-59 planets also fall within a flux regime that means that they are interesting case studies in assessing the atmospheric evolution for terrestrial planets in the presence of a relatively high XUV environment.

Herein, we explore the potential for atmospheric detection and characterization across a range of varying scenarios for L 98-59 b, c, and d. The feasibility of atmospheric characterization is determined first by selecting the most favorable instruments to conduct transit spectroscopy measurements of each planet. Theoretical observations of the planets are

conducted using HST to determine what we could detect in the near-term, while simulated JWST observations look into the possibilities of the intermediate future. The atmospheres considered here do not represent the full spectrum of potential outcomes but are merely a representation of atmospheres that have been motivated by their ability to produce measurable spectra, given the known planetary parameters.

The structure of the paper is as follows. Section 2 provides a detailed overview of the methods and inputs considered in the simulation of spectra using HST and JWST. Section 3 considers the prospective atmospheric detection that can be carried out with HST, while Section 4 explores the atmospheric signatures that will be targets of interest for near-future characterization with JWST. A discussion of the results can be found in Section 5, with conclusions following in Section 6.

2. Methods

In the following subsections, we describe our methods for assessing the detectability and signal-to-noise ratio (S/N) of various spectral signatures for the L 98-59 system with numerous instruments and observational modes available to HST and JWST. The elemental and molecular composition of each planetary environment is simulated and analyzed using the Planetary Spectrum Generator (PSG), an online¹⁴ radiative-transfer suite that computes synthetic transit spectra for a wide range of planetary atmospheres (Villanueva et al. 2018). We aim to determine how feasible the detection and characterization of atmospheres dominated by H₂ or H₂O would be for HST, and we assess how the detection may be improved with observations via JWST. Simulated JWST observations also include scenarios where the atmospheres are dominated by CO₂ or O₂, representing post-runaway and/or desiccated states. In some cases, we also include the presence of aerosols. We consider an atmosphere to be detected when sufficient S/N is achieved on the strongest molecular feature in the spectrum at a 5 σ confidence level. All simulations include a panel that details the relative contribution of each molecule to the overall spectrum of the atmosphere. These spectra are calculated by subtracting the spectrum without the molecule from the full spectrum.

2.1. Simulating Transit Spectra with PSG

Our transit simulated spectra with PSG integrate molecular and aerosol extinctions via accurate spectroscopic methods and parameters, which include a realistic treatment of the radiative transfer in layer-by-layer pseudospherical geometry. For this investigation, the molecular spectroscopy is based on the latest HITRAN database (Gordon et al. 2017) integrated via the correlated-k method, which is complemented by UV/optical data from the Max Planck Institute of Chemistry database (Keller-Rudek et al. 2013). In addition to the collision-induced absorption (CIA) bands available within the HITRAN database, the MT_CKD water continuum is characterized as H₂O–H₂O and H₂O–N₂ CIAs (Kofman & Villanueva 2021). The PSG also includes a large database of scattering and absorptive properties from many known aerosols—both measured in situ on Earth and laboratory-measured values for other solar system materials—that can be added ad hoc to any synthetic transit spectrum. Further details on the treatment of

Table 1
Stellar and Planetary System Parameters Modeled

Stellar Parameter	Modeled		
Spectral type	M3V		
Mass (M_{\odot})	0.312 \pm 0.031		
Radius (R_{\odot})	0.314 \pm 0.014		
Effective temperature (K)	3412 \pm 49		
J (mag)	7.933 \pm 0.027		
Planetary Parameter	L 98-59 b	L 98-59 c	L 98-59 d
Semimajor axis (au)	0.02282	0.0317	0.0506
Mass (M_{\oplus})	0.45	2.42 \pm 0.35	2.31 \pm 0.46
Radius (R_{\oplus})	0.80 \pm 0.05	1.35 \pm 0.07	1.57 \pm 0.14
Orbital period (days)	2.2531	3.6904	7.4512
Transit duration (hr)	1.02	1.24	0.91
Inclination (deg)	88.7	89.3	88.5
Equilibrium temperature ($A = 0.3$) (K)	558	473	374
Insolation (S_{\oplus})	23.9	12.4	4.85
Mean density (g cm^{-3})	4.9	5.4	3.3
Surface gravity (m s^{-2})	6.9	13.1	9.2

aerosols for the simulations presented here can be found in Section 2.4. In generating each spectrum, we input the basic parameters of the star and each planet, summarized in Table 1. Planetary atmospheres are designed by adjusting a range of parameters fully described in Section 2.3.

2.2. Stellar and Planetary Parameters

In all simulations, planetary parameters are derived from the system’s discovery (Kostov et al. 2019a), as well as Cloutier et al. (2019), whose work constrained the masses for each planet. Current radial velocity measurements only provide an upper limit for the mass of L 98-59 b of $<1.01 M_{\oplus}$; here we assume 0.45 M_{\oplus} , or 2.70×10^{24} kg for an Earth-like bulk composition (Lopez & Fortney 2014). For planetary studies, the planetary equilibrium temperature is estimated assuming either an Earth-like Bond albedo of $A = 0.3$ or an unrealistic $A = 0.0$ (e.g., Borucki et al. 2012; Anglada-Escudé et al. 2016; Dittmann et al. 2017; Gillon et al. 2017). For planets orbiting an M dwarf, the Bond albedo would be lower than the equivalent planet placed around a Sun-like star. This is because of the IR shift of the incident spectrum, which would be less efficiently scattered or reflected by most plausible planetary atmospheres. Here we use the Earth Bond albedo value of $A = 0.3$, keeping in mind that this is a nominal estimate. A summary of the stellar and planetary system parameters as model inputs for each simulation is shown in Table 1.

2.3. Atmospheric Parameters

This work considers four potential planetary environments, each varying in elemental composition, while some expand to include additional caveats, such as the presence of clouds and hazes. For all three planets, we simulate clear and cloudy steam atmospheres, desiccated atmospheres composed of O₂/O₃, and clear and cloudy Venus-like atmospheres dominated by CO₂. An additional clear low mean molecular weight atmosphere is also simulated for L 98-59 c and d.

The structure of the atmosphere is described in PSG layer by layer, with information for each layer including pressure (bars), temperature (K), molecular abundances (molecules

¹⁴ The PSG is available at <https://psg.gsfc.nasa.gov/>.

Table 2
Atmospheric Parameters Modeled

Atmospheric State	Aerosols	Gases	MMW (g mol ⁻¹)	Surface Pressure (bars)
H ₂ -dominated	None	83.7% H ₂ , 16.2% He, trace gases ^{a,b}	2.36	1
Steam, clear sky	None	90% N ₂ , 10% H ₂ O	18.02	1
Steam, hazy	Titan tholins	90% N ₂ , 10% H ₂ O, trace organic haze	18.02	1
CO ₂ -dominated, clear sky	None	96.5% CO ₂ , 3.6% N ₂ , trace gases ^c	44	92
CO ₂ -dominated, cloudy	H ₂ SO ₄ clouds	96.5% CO ₂ , 3.6% N ₂ , trace gases ^d	44	92
O ₂ -desiccated	None	99.9% O ₂ , trace O ₃ ^e	32	1, 10

Notes.

^a L 98-59 c: 663.6 ppm H₂O, 488.3 ppm CH₄, trace CO, CO₂, O₂.

^b L 98-59 d: 692.7 ppm H₂O, 488.5 ppm CH₄, trace CO, CO₂, O₂.

^c Trace CO, H₂O, SO₂, O₂, O₃.

^d Trace CO, H₂O, SO₂, O₂, O₃, H₂SO₄.

^e See Figure 7.

molecule⁻¹), and aerosol abundances (kg kg⁻¹) with respect to the total gas content. Altitudes are computed employing the hydrostatic equation. Computation of layer-by-layer integrated column densities (molecules m⁻²) and aerosol mass densities (kg m⁻²) are then computed along the transit slant paths employing a pseudospherical geometry. With no constraints on planetary surface temperatures, some simulations use an isothermal temperature profile set at the planetary equilibrium temperature. We note that this method is conservative, as it does not account for possible additional heat sources or temperature inversion and results in a possible underevaluation of the atmospheric scale height.

Each atmosphere is configured with varying inputs.

1. H₂-dominated. The pressure/temperature (P/T) profiles are calculated based on a nongray analytical model (Parmentier et al. 2014) according to the planet's equilibrium temperature and gravity. Molecular abundances are then derived layer by layer by considering the equation of state (EOS) and chemical equilibrium computed by Kempton et al. (2017), which does not include disequilibrium chemistry or photochemistry. The resulting atmosphere is detailed in Table 2, and the concentrations of H₂O and CH₄ remain nearly constant (within 20 ppm) over altitude. Each simulation is representative of a cloud-free atmosphere.
2. Steam atmosphere. For a water-rich steam atmosphere, we assume purely radiative, isothermal atmospheric cases with and without the presence of aerosols. Previous studies have used this isothermal approximation only for the mesosphere and above (Kasting 1988; Kopparapu et al. 2013; Leconte et al. 2013a; Marcq et al. 2017; Turbet et al. 2019). Even if the surface temperature is extremely hot, the top of the atmosphere (TOA) temperature is always fairly cold. Since we are not using a climate model to predict the tropospheric temperature, we have extended this approximation to the troposphere as well. This should not have an impact on the transmission spectra because in a hot and moist atmosphere, the lowest layers are opaque to infrared radiation and therefore could not be probed using transmission spectroscopy. The volume mixing ratios of H₂O and N₂ are kept constant, and the values are shown in Table 2. In simulations where aerosols are included, their treatment is summarized in Section 2.4. We also note that the temperature of the isotherm in the

mesosphere and above would likely be higher than the planet's equilibrium temperature that we have assumed in this work. Thus, we may have underestimated the scale height and atmospheric transit depth for steam atmospheres.

3. Post-runaway greenhouse. Venus-like atmosphere with a provided vertical profile dominated by CO₂ is simulated from the use of a preloaded template in PSG, whose parameters are derived from Ehrenreich et al. (2012), Bierson & Zhang (2020), and Vanaele (2020). To approximate the temperature of the tropopause, we set the TOA to each planet's skin temperature ($T_s = T_{eq} \left(\frac{1}{2}\right)^{1/4}$, $b = 469$ K, $c = 398$ K, $d = 315$ K). In the clear case, the volcanic aerosols included in the cloudy case from Palmer & Williams (1975) are removed. For simulations where aerosols are included, their treatment is summarized in Section 2.4.
4. O₂-desiccated. For a post-runaway desiccated planet, we assume an isothermal atmosphere that is rich in abiotic O₂, where we expect to see O₃ formation from the photochemical processing of this O₂. To properly account for the amount of O₃ present in the atmosphere, we use the photochemical module of Atmos, a coupled 1D photochemical climate model (Arney et al. 2016). Its photochemical module is based on a code originally developed by Kasting et al. (1979) and has been significantly modernized as described in Zahnle et al. (2006). The photochemical model has been additionally updated as described in Lincowski et al. (2018), where it has also been validated on Earth and Venus. We assume an atmosphere dominated by O₂ with trace amounts of O₃ (calculated by the model) and no other gases. We consider total pressures of 1 and 10 bars. Because no complete calibrated stellar spectrum of L 98-59 is available, for the purposes of modeling the photochemistry of these O₂-rich atmospheres only, we substitute as the input stellar spectrum the panchromatic spectrum of GJ 581 (also M3V) from the MUSCLES Survey (v21; France et al. 2016; Loyd et al. 2016; Youngblood et al. 2016) scaled to the flux given in Table 1. The output chemical profiles from Atmos are then provided to PSG to construct a simulated spectrum.

A summary of the atmospheric parameters as model inputs for each simulation is shown in Table 2. We include the atmospheric state modeled, present aerosols and gases, mean

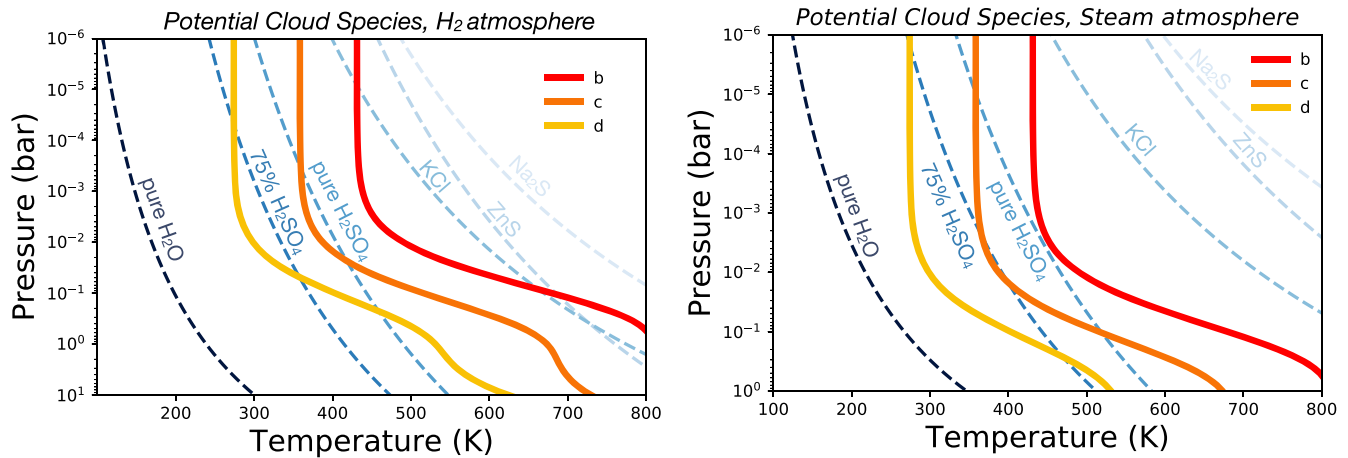


Figure 2. Temperature–pressure profile models of each planet in the L 98-59 system compared to theoretical cloud vapor pressure curves. Where a planet profile crosses a vapor pressure curve, cloud condensation is expected. Left: solar-metallicity profiles and saturation curves. Right: water-rich profiles and cloud curves.

molecular weight (MMW) of the atmosphere, and surface pressure.

2.4. Treatment of Clouds/Hazes

Both clouds and hazes are ubiquitous throughout the solar system, while their presence on various exoplanets is widely inferred from observations (e.g., Kreidberg et al. 2014). However, the treatment of clouds and hazes in atmospheric models for transit spectra simulations varies greatly, from fully self-consistent photochemical models (e.g., Morley et al. 2015; Lincowski et al. 2018; Meadows et al. 2018a) to highly parameterized scattering functions (e.g., Sing et al. 2016). By integrating the layer-by-layer aerosol abundances (kg kg^{-1}) and spectroscopic scattering models, PSG solves for the radiative transfer across the line of sight. For aerosols employing the HITRAN Refractory Index (HRI; Massie & Hervig 2013) database, PSG utilizes precomputed Mie scattering models for different particle sizes in the form of Henyey–Greenstein coefficients (Henyey & Greenstein 1941), which are internally expanded into Legendre coefficients to be ingested by the radiative-transfer suite. Laboratory results for the optical properties of exoplanet hazes do not yet exist, so in this work, we include clouds and hazes in our models that have direct solar system analogs or from which we approximate based off solar system analogs together with existing laboratory results on particle size, chemistry, and production rate for exoplanet hazes.

For CO_2 atmospheres, we use the refractive indices of Palmer & Williams (1975) for sulfuric acid at 75% concentration for Venus-like clouds in PSG, placing clouds between 1 and 0.01 bar at 1 kg m^{-3} mass density with particle sizes of $1 \mu\text{m}$. These values follow from Figure 1 of Lebonnois & Schubert (2017), which provides a model of the vertical structure of Venus’s atmosphere. Here we choose to use Venus’s clouds as a possible representative case for a lack of other constraints. Venus-like clouds are a potentially pessimistic case, as the high irradiance of the L 98-59 planets may cause true Venus clouds to burn off and dissipate more readily than in the upper atmosphere of Venus itself. However, recent laboratory results regarding haze formation in warm CO_2 atmospheres suggests high sulfuric acid production, which could give rise to clouds (Vuitton et al. 2021). We also note that the formation of sulfuric acid clouds requires the presence

of trace amounts of H, which may have escaped from this atmosphere. Nevertheless, we use such clouds in our cloudy CO_2 PSG simulations to explore the effect reasonable clouds might have on observations made by JWST.

We show in Figure 2 the saturation vapor pressure profiles (derived following Morley et al. 2013) of pure water, pure H_2SO_4 , a 75% sulfuric acid concentration, KCl, ZnS, and Na_2S , together with parameterized temperature–pressure profiles of the three L 98-59 planets. Of all known potential cloud species, only some sulfuric acid clouds (with some level of water concentration) are likely to form in the atmospheres of these planets, which is why we include them in our pessimistic cloudy case for a CO_2 atmosphere. We use these models as a guide for which cloud species to consider, rather than a self-consistent framework upon which to model clouds. If a saturation vapor pressure curve is crossed, the potential for such clouds exists, but we do not prescribe where they must be in the atmosphere. Even if clouds form lower in the atmosphere than observations probe, atmospheric mixing may loft them to higher altitudes where they may impact observations (Morley et al. 2013). Saturation vapor pressure profiles are metallicity-dependent; therefore, ZnS or KCl clouds could be possible for L 98-59 b in a solar-metallicity atmosphere (Figure 2, left). However, L 98-59 b is unlikely to retain such an H_2 -rich atmosphere (Section 3.1), and the temperature–pressure profile of a high-metallicity, H_2O - or CO_2 -rich L 98-59 b does not cross the curves of these cloud species at all (Figure 2, right). Given these considerations, we do not consider KCl or ZnS cloud species in our models.

For steam atmospheres, laboratory experiments have shown substantial haze production (Hörst et al. 2018), and the compositions of these hazes appear to be complex organics (Moran et al. 2020). For hazes in steam atmospheres, we use the refractive indices of Khare et al. (1984) for Titan-based organic haze, which are preloaded in PSG from the HRI database. The atmospheric parameters for Titan are derived from Teanby et al. (2006). The Khare et al. (1984) measurements are one very specific outcome of haze formation and composition produced via a room-temperature 90% N_2 , 10% CH_4 experiment done under an ambient Earth atmosphere. Therefore, it should be treated with heavy skepticism as a basis for extrapolation to exoplanet atmospheric hazes. However, as there are currently no laboratory measurements of optical properties of any exoplanet hazes relevant to the bulk

atmospheric compositions explored here, the use of Khare et al. (1984) was chosen as a necessary proxy, with the caveat that further measurements and models should be performed as additional theoretical data become available. Laboratory measurements specific to exoplanets like L 98-59 will be required to make true interpretations of atmospheric observations, rather than the exploration of generally reasonable but unconstrained scenarios, as we have done in this work. We do not explore condensation clouds in steam atmospheres because of the temperature regimes encompassed by the atmospheres of the L 98-59 planets. The planetary atmospheres, even high in the atmosphere, never get cool enough for water clouds to condense, and other cloud species (i.e., those shown by other works, such as Morley et al. 2013) form only at hotter temperatures in a higher-metallicity steam atmosphere, as we show in Figure 2.

We choose not to include any aerosols in either our H₂ atmospheres or our desiccated O₂ atmospheres. Laboratory results have shown that hydrogen atmospheres have poor haze production efficiency in comparison to atmospheres dominated by H₂O or CO₂ (Hörst et al. 2018), and previous modeling work shows that the amount of haze needed in hydrogen atmospheres to significantly impact observations of terrestrial planets is unrealistic (Moran et al. 2018). While previous studies considered KCl or ZnS clouds in H₂ atmospheres (Morley et al. 2013), more recent work shows that only silicate clouds are likely to substantially impact the spectra of H₂ atmospheres due to nucleation energy barriers for salt cloud formation (Gao et al. 2020), in addition to this only being relevant for L 98-59 b. As none of the L 98-59 planets are hot enough for silicate cloud formation, we ignore clouds for our H₂ atmospheres. Although further observations are required to evaluate whether haze formation is efficient or inefficient in H₂ atmospheres, the detection or absence of N₂-N₂ or N₂-X CIA features may help distinguish between types of atmospheres that are dominated by either hazy H₂ or N₂-H₂O (Schwieterman et al. 2015). For O₂ atmospheres, we do not include aerosols because we find no photochemical modeling results, laboratory results, or solar system analogs upon which to base a possible aerosol layer in a desiccated O₂ atmosphere. However, this may be an interesting avenue to explore in future work.

2.5. Instrumental Parameters and Sensitivity Analysis

Once the atmospheric framework for the planet of interest is selected, PSG can be used to model the instrument parameters for any given observatory. Each telescope and instrument considered in this work uses the input parameters defined by the database of preloaded models within PSG. The PSG accounts for system throughput and presents the user with a table that describes these values, all of which are found in the instrument and detector parameters. This work uses PSG to model transmission spectroscopy observations specifically using multiple instruments from HST and JWST. Although fringing and other systematic sources of noise have been identified in these observational modes, their overall effect on the actual reduced data are not yet sufficiently quantified, and these effects were not included in our noise simulator and could lead to an overestimation of the S/N (see Section 5.3). We have benchmarked PSG’s noise simulator by validating our JWST models against PandExo (Batalha et al. 2017), where we find PSG and PandExo to be within 10% agreement for all JWST instruments.

Instrumental inputs include the following.

1. HST/WFC3. Simulated observations of transmission spectroscopy with HST are conducted using the near-infrared (NIR; 1.1–1.7 μm) G141 grism on the Wide-Field Camera 3 (WFC3) instrument ($R = 130$).
2. JWST/NIRISS SOSS. Modeled simulations of exoplanet atmospheres show that observations with the Near-Infrared Imager and Slitless Spectrograph (NIRISS) operating in Single Object Slitless Spectroscopy (SOSS; $R = 700$) are required to cover the 0.6–2.8 μm wavelength range for targets that are too bright to be observed with NIRSpec Prism, which would be saturated in one read of the detector when observing a star as bright as L 98-59 ($K = 7.1$; Batalha & Line 2017).
3. JWST/NIRSpec G395H. To simulate spectral features within the 2.87–5.14 μm wavelength range, we use NIRSpec with the G395H disperser ($R = 2700$), as an observation with both NIRISS and NIRSpec G395H yields the highest-content spectra with the tightest constraints (Batalha & Line 2017).
4. JWST/MIRI LRS. Beyond the extent of NIRISS/NIRSpec’s wavelength range, certain gaseous features, such as the O₂-O₂ CIA feature at 6.4 μm , are only accessible through use of the Mid-InfraRed Instrument (MIRI; Bouchet et al. 2015) low-resolution spectrometer (LRS; $R = 100$; Kendrew et al. 2015). MIRI LRS has both a camera and a spectrograph that perform in the wavelength range of 5.0–28.0 μm , with transit observations ending at 12.0 μm .

For the sensitivity analysis, PSG includes a noise calculator that accounts for the noise introduced by the star or source itself (N_{source}) and the background noise (N_{back} ; e.g., zodiacal dust) following a Poisson distribution with fluctuations depending on \sqrt{N} , with N the mean number of photons received; the noise of the detector (N_D); and the noise introduced by the telescope (N_{optics}). The total noise is then defined as $N_{\text{total}} = \sqrt{N_{\text{source}} + 2(N_{\text{back}} + N_D + N_{\text{optics}})}$.

In all synthetic spectra shown within this work, the resolving power ($R = \lambda/\Delta\lambda$) selected for each HST and JWST instrument is varied to accommodate the most efficient detection of the strongest molecular feature found within the spectrum of a given atmosphere based on Table 4 in Wunderlich et al. (2019). The chosen R value for a specific detection is noted in the results (Tables 3 and 4). To calculate the S/N and the number of transits needed for a 5σ detection, the resolving power is optimized by adjusting the binning of the strongest feature in each simulation to maximize its S/N.

The S/N (given as “SNR” in the following equations) is calculated by subtracting the nearest continuum value from the highest value of any given spectral band. This value, considered the “relative depth” of a feature, therefore differs between the visible (VIS; dominated by the Rayleigh slope), NIR, and mid-infrared (MIR). The relative depth can then be divided by the noise value at the given band to determine the S/N. For a source-dominated noise limit, the number of transits needed to achieve an $X\sigma$ detection is computed as

$$N_{\text{transits}}^{X\sigma} = N_i^* (X/\text{SNR}_i)^2, \quad (1)$$

where $X\sigma$ is the confidence level of value X , and N_i is the initial number of transits at which SNR_i is computed. If SNR_i is estimated from one transit, $N_i = 1$ and Equation (1) can be

Table 3
The Modeled Observability of HST within This Study

Planet	L 98-59 b	L 98-59 c	L 98-59 d
Instrument	WFC3 ($R = 30$)		
Atmosphere	H_2 -/He-dominated		
Spectral feature	H_2O 1.38 μm		
(S/N)-1	...	10	13
N transits (5σ)	...	1	1
Spectral feature	CH_4 1.68 μm		
(S/N)-1	...	11	13
N transits (5σ)	...	1	1
Atmosphere	Steam		
Spectral feature	H_2O 1.38 μm ; clear		
(S/N)-1	3.0	2.1	2.0
N transits (5σ)	3	6	5
Spectral feature	H_2O 1.38 μm ; hazy		
(S/N)-1	1.7	1.1	1.2
N transits (5σ)	9	20	17

simplified as

$$N_{\text{transits}}^{X\sigma} = (X/\text{SNR}_i)^2. \quad (2)$$

3. Prospects and Results for Characterization with HST

Thus far, HST atmospheric follow-up of small planets has focused on detecting the broad water peak at 1.4 μm with HST's WFC3 IR grisms (e.g., GJ 436b, Knutson et al. 2014a; HD 97658b, Knutson et al. 2014b; GJ 1214b, Kreidberg et al. 2014; GJ 1132b, Southworth et al. 2017; TRAPPIST-1, de Wit et al. 2016, 2018; GJ 3470 b, Benneke et al. 2019a; K2-18b, Benneke et al. 2019b; Tsiaras et al. 2019; HD 106315c, Kreidberg et al. 2020; HD 3167c, Mikal-Evans et al. 2021; and LHS 1140 b, Edwards et al. 2021). However, this method of exploring whether or not such worlds have atmospheres or, further, what the chemical constituents of these atmospheres are has been plagued by weak, muted molecular features due to either high mean molecular weight atmospheres or high cloud decks (e.g., Sing et al. 2016; Wakeford et al. 2019b). Although planets with detected hydrogen envelopes are slightly larger ($>2 R_{\oplus}$) than the planets in the L 98-59 system, transit observations with HST would provide a first look at determining whether or not these planets contain atmospheres. With current ongoing efforts through HST's general observer (GO) program, we soon expect to place these initial constraints on L 98-59 b–d (HST-GO-15856 and HST-GO-16448; PI: Barclay) and specifically constrain abundances if they are dominated by abundances of H_2 or H_2O .

In the following subsections, we present simulated transmission spectra of each planet via WFC3. Details on S/N and transit values for individual spectral features are found in Table 3.

3.1. Detecting a Low Mean Molecular Weight Atmosphere with HST

Hitherto, atmospheric characterization of exoplanets has revealed an abundance of close-in planets with atmospheres holding substantial amounts of hydrogen/helium. While small

Table 4
JWST Instruments and Their Observability in This Study

Planet	L 98-59 b	L 98-59 c	L 98-59 d
Instrument	NIRSpec G395H		
Atmosphere	Venus-like ($R = 30$)		
Spectral feature	CO_2 4.3 μm ; clear		
(S/N)-1	1.3	0.98	1.2
N transits (5σ)	16	26	17
Spectral feature	CO_2 4.3 μm ; cloudy		
(S/N)-1	0.83	0.56	0.66
N transits (5σ)	37	80	57
Instrument	NIRISS SOSS		
Atmosphere	Steam ($R = 23$)		
Spectral feature	H_2O 1.38 μm ; clear		
(S/N)-1	8.7	6.1	6.8
N transits (5σ)	1	1	1
Spectral feature	H_2O 1.38 μm ; hazy		
(S/N)-1	5.4	3.8	3.9
N transits (5σ)	1	2	2
Atmosphere	O_2/O_3 -desiccated ($R = 20$)		
Spectral feature	O_2 CIA 1.27 μm , 1 bar, 200 K		
(S/N)-1	0.68	0.67	0.9
N transits (5σ)	55	57	31
Spectral feature	O_2 CIA 1.27 μm , 10 bars, 200 K		
(S/N)-1	0.95	0.67	0.9
N transits (5σ)	28	57	31
Spectral feature	O_2 CIA 1.27 μm , 1 bar, equilibrium temp.		
(S/N)-1	1.3	1.1	1.5
N transits (5σ)	16	20	12
Spectral feature	O_2 CIA 1.27 μm , 10 bars, equilibrium temp.		
(S/N)-1	3.0	2.1	2.0
N transits (5σ)	3	6	7
Instrument	MIRI		
Atmosphere	O_2/O_3 -desiccated ($R = 10$)		
Spectral feature	O_2 CIA 6.4 μm , 1 bar, equilibrium temp.		
(S/N)-1	0.71	0.62	0.8
N transits (5σ)	50	65	40
Spectral feature	O_2 CIA 6.4 μm , 10 bars, equilibrium temp.		
(S/N)-1	1.5	1.1	1.0
N transits (5σ)	12	23	24
Spectral feature	O_3 9.7 μm , 10 bars, equilibrium temp.		
(S/N)-1	0.84	0.78	0.9
N transits (5σ)	36	41	32

planets are unlikely to retain primordial hydrogen-rich atmospheres (Rogers 2015; Fulton et al. 2017), secondary atmospheres could form from volcanic outgassing or delivery of volatiles from comets. The presence of exoplanets with volatile atmospheres at short orbital periods raises the question as to whether these atmospheres are stable (Koskinen et al. 2007). For hydrogen-dominated atmospheres, the high UV flux close to the star dissociates the molecular hydrogen, resulting in atomic hydrogen dominating the upper regions (Yelle 2004; García Muñoz 2007). In these atomic regions, heating typically

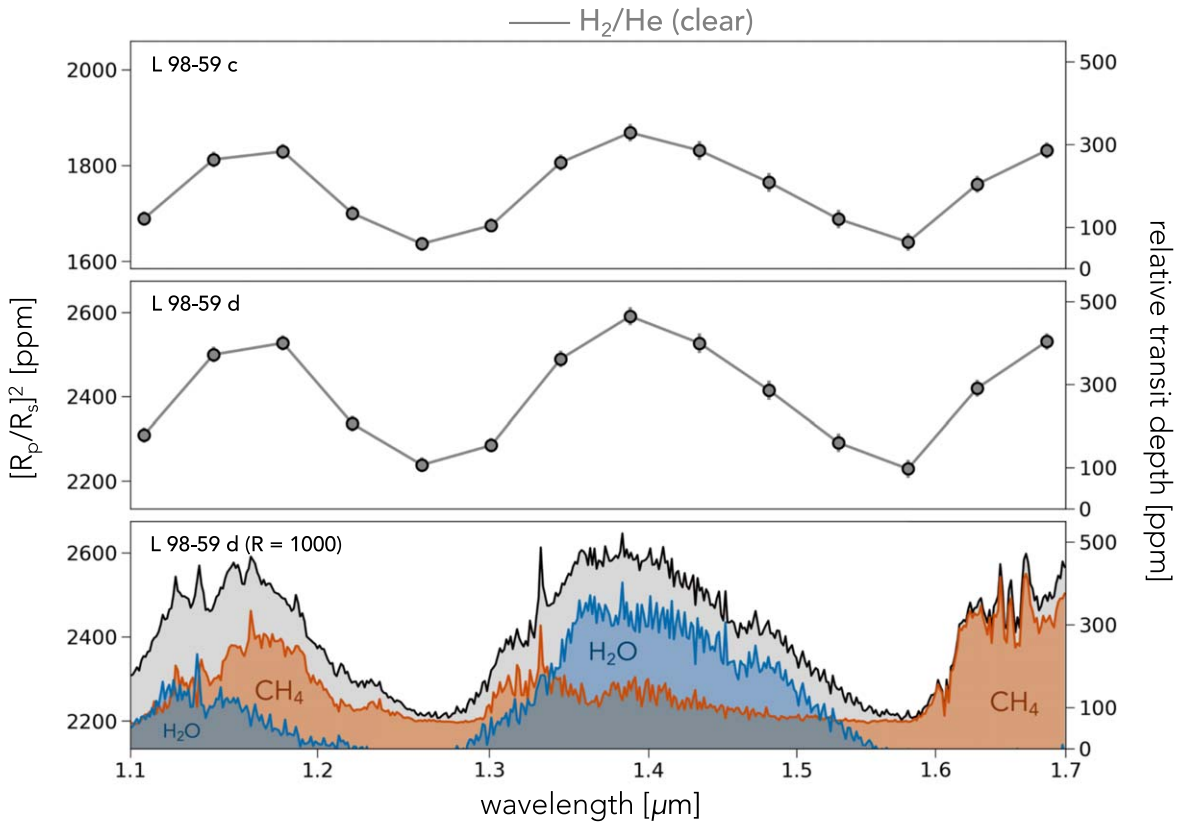


Figure 3. One transit of an H₂-/He-dominated atmosphere simulated with HST/WFC is shown for L 98-59 c (top) and L 98-59 d (middle) in gray. Error bars are shown for observations simulated at $R = 30$. The gaseous species corresponding to the molecular features in each planetary spectrum are shown (bottom) at a higher ($R = 1000$) resolution. Here the black line represents the corresponding simulated spectrum for L 98-59 d (middle), while the gray shading indicates the sum of all gases present. The absorption of H₂O is shown in blue and CH₄ in orange.

results in gas temperatures on the order of 5000–10,000 K. At such high temperatures, the upper atmospheres of close-in exoplanets are weakly bound, and the gas becomes more susceptible to escaping the planet’s gravity. In many cases, and especially for small, low-mass planets such as those within the L 98-59 system, the total time-integrated high-energy flux (high-energy exposure) a planet receives over its lifetime of billions of years is a significant fraction of its gravitational binding energy (Lecavelier Des Etangs 2007). This available energy means that unlike solar system planets, where atmospheric escape is vital for shaping the chemical evolution of a planet’s atmosphere (Lammer et al. 2008), atmospheric escape can affect the evolution of a planet’s bulk composition for close-in exoplanets. Modeling work suggests that this atmospheric escape is a strong driver in the evolution of many close-in planets (Owen 2019).

To determine the plausibility of each planet holding an atmosphere dominated by hydrogen, we set the rms velocity of H₂ equal to the escape velocity of the planet. The following formula is used to calculate the escape temperature of H₂ for each given planet, based on its size:

$$T_{\text{esc}} > \frac{1}{54} \frac{GM_p m}{kR_p}. \quad (3)$$

Due to its low expected gravity, an H₂ atmosphere on L 98-59 b would be highly vulnerable to atmospheric escape (see Figure 1). When considering a Bond albedo = 0.3, a calculation of the escape temperature of hydrogen on L 98-59 b shows that the equilibrium temperature (558 K) is higher than

the escape temperature of H₂ molecules (342 K) and thus it is not likely that the planet retains such an atmosphere. For this reason, an H₂-dominated atmosphere on L 98-59 b is not investigated within this work. However, the equilibrium temperatures of L 98-59 c and d (473 and 374 K, respectively) allow for retention of secondary H₂ atmospheres, given that their equilibrium temperatures are lower than their escape temperatures for H₂ (509 and 402 K, respectively).

Figure 3 shows the simulated spectrum for one transit of a clear atmosphere dominated by H₂/He for L 98-59 c and L 98-59 d. The bottom panel accompanies these spectra to show the detailed molecular composition of each planetary atmosphere, using L 98-59 d as an example. Although the atmospheres contain a multitude of trace gases (Table 2), only H₂O and CH₄ are shown individually, as they are primarily responsible for creating the absorption features visible in each modeled spectrum.

On L 98-59 c and d, a clear-sky atmosphere dominated by H₂/He has multiple spectral features that can be detected and characterized with WFC3. Although the features found in the 1.1–1.3 μm range are blended by H₂O and CH₄, the peaks at 1.38 and 1.68 μm can be attributed to the absorption of H₂O and CH₄, respectively. These peaks provide ample signal in both planets, notably for L 98-59 d, whose lower density increases the S/N and scale height substantially. In a single transit, HST could potentially rule out a featureless transmission spectrum on such an atmosphere for both planets with a 5σ confidence level and $S/N \geq 10$, providing ample information for a minimal allocation of time. Moreover, a physically

realistic amount of cloud and/or haze in an H_2 atmosphere is anticipated not to mute features beyond HST’s capabilities (Moran et al. 2018).

3.2. Detecting H_2O with HST

Beyond the ability to detect the presence of an atmosphere or rule out the possibility of one dominated by H_2/He , HST observations may be used to detect H_2O absorption in a steam atmosphere. It is of particular interest to investigate this possibility on L 98-59 b, where the mean molecular weight of a steam atmosphere makes it much more resilient to atmospheric escape in comparison to one dominated by H_2 . While H_2 -dominated sub-Neptunes with equilibrium temperatures similar to L 98-59 b ($T_{eq} \sim 558$ K) are sometimes cloudy/hazy (e.g., as in the case of GJ 1214 b; Kreidberg et al. 2014), a steam atmosphere on the terrestrial L 98-59 b would likely be very different. An outgassed atmosphere from a volatile-rich surface would have few trace species (e.g., Na_2S , KCl) that condense at these temperatures to form clouds (and the atmosphere is likely too hot for water itself to condense; Morley et al. 2013). While lab experiments for colder steam atmospheres show substantial haze production rates (Hörst et al. 2018), no lab experiments exist yet for hotter steam atmospheres.

In contrast to the active M dwarf TRAPPIST-1, the host star in the L 98-59 system shows no evidence for stellar activity in the TESS data (Kostov et al. 2019b) and is likely a relatively quiet M dwarf with a low level of XUV activity. Such stars typically have X-ray activity of $L_x \approx 10^{-4.5} L_{bol}$ (Shkolnik & Barman 2014). Using this activity level and scaling from the TRAPPIST-1 planet escape simulations of Bolmont et al. (2017), we estimate that a steam atmosphere on L 98-59 b would lose \sim seven Earth ocean equivalents per gigayear. This is orders of magnitude below the inferred water mass fraction of the planet—assuming bulk composition similar to those previously inferred for the TRAPPIST-1 planets (Grimm et al. 2018; Agol et al. 2021)—illustrating that H_2O can still be present in the atmosphere of L 98-59 b, which has the highest anticipated transmission spectroscopy S/N of any planet smaller than $1.8 R_{\oplus}$ of those discovered thus far. While L 98-59 b receives \sim 23 times Earth’s incident flux, the detection of molecular absorption features on such a highly irradiated planet would be greatly significant, as it would suggest that M dwarf planets can readily retain their atmospheres.

Moreover, terrestrial planet formation simulations predict a wide variety of possible water abundances of up to many thousands of Earth oceans, and water mass fractions of \sim 1%–10%, particularly for systems like the planets of L 98-59 and TRAPPIST-1 that are close to mean-motion resonance around an M dwarf, are suggestive of planet migration (e.g., Chambers 2001; Hansen & Murray 2012; Mordasini et al. 2012; Tian & Ida 2015; Unterborn et al. 2018). The recent update in TTVs measured for the TRAPPIST-1 system (Agol et al. 2021) has strongly revised the estimated water mass fractions for the inner planets b, c, and d, from \gtrsim 5% (Grimm et al. 2018) down to \lesssim 0.01%, several times lower than Earth’s ocean water mass fraction. However, this estimation is still consistent with significant water vapor in the planetary atmospheres.

Figure 4 shows model spectra of both a clear and a hazy steam atmosphere with simulated HST/WFC3 observations for L 98-59 b, L 98-59 c, and L 98-59 d. The bottom panel

accompanies these spectra to show the detailed molecular composition of each hazy steam atmosphere, using L 98-59 d as an example. The blue models show a clear sky spectrum with large H_2O absorption features and data uncertainties calculated for a 5σ detection of the strongest spectral feature. The green models include Titan-based organic haze whose refractive indices are derived from Khare et al. (1984), with data uncertainties calculated for a 5σ detection of the same spectral feature.

The clear steam atmosphere (blue) has a strong H_2O absorption feature at $1.38 \mu m$ that can be detected at 5σ in three, six, and five transits for L 98-59 b, c, and d, respectively. However, when considering the presence of a Titan-like haze (green), the number of transits required to detect the same $1.38 \mu m$ absorption feature at 5σ more than doubles for each planet, requiring 9, 20, and 17 transits for L 98-59 b, c, and d, respectively. This decrease in sensitivity can be attributed to the continuum level in our modeled spectra that is set by Titan’s high-altitude haze (Robinson et al. 2014), whose placement will have more dramatic effects at UV/VIS/NIR wavelengths, where the haze particles are strongly absorbing (Tomasko et al. 2008). The increase in haze production as we move out of the system indicates a link between aerosol formation and equilibrium temperature predicted by theoretical models for warm Neptune and super-Earth planets (Fortney et al. 2013; Morley et al. 2015). Crossfield & Kreidberg (2017) hypothesized that the size of the water absorption feature of an exoplanet in the WFC3 bandpass may be related to the equilibrium temperature of the planet. When considering warm Neptunes, hotter planets appear to have larger observable features, whereas cooler planets are able to more efficiently form high-altitude aerosol layers, muting these absorption features. The resulting flattened spectra that can be attributed to high-altitude aerosol layers have been observed with WFC3 for large-mass low-density planets (Libby-Roberts et al. 2020), but additional observations will be required to confirm or refute this trend for both mini-Neptune and terrestrial planets.

4. Prospects and Results for Future Characterization with JWST

One of the first planetary systems characterized by JWST will be L 98-59. JWST’s Guaranteed Time Observations (GTO) include transits for L 98-59 c (NIRISS SOSS, one transit, program number 1201; PI: Lafreniere) and L 98-59 d (NIRSpec/G395H, 2 transits, program number 1224; PI: Birkmann; NIRISS SOSS, one transit, program 1201; PI: Lafreniere). Therefore, simulated transit observations of the L 98-59 planets using these JWST instruments are timely. If HST observations indicate that the planets in the L 98-59 system lack low mean molecular weight gases, this motivates the follow-up search for secondary atmospheres dominated by high mean molecular weight species such as CO_2 or O_2 to be the primary constituent of some or all of the planetary atmospheres in this system.

In the following subsections, we present model transmission spectra of each planet using NIRISS SOSS, NIRSpec/G395H, and MIRI LRS. Details on S/N and transit values for individual spectral features are found in Table 4.

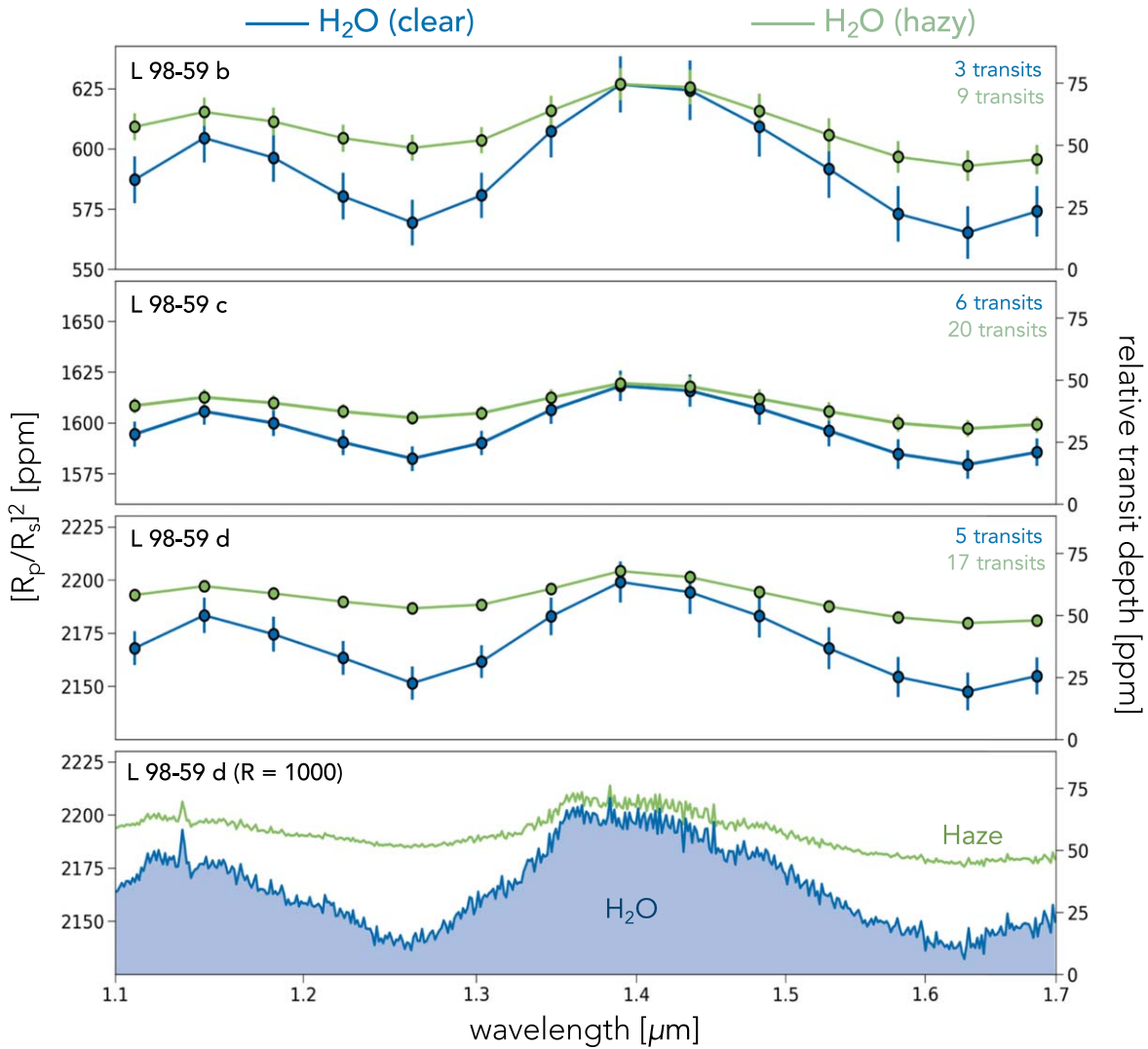


Figure 4. Simulated HST/WFC3 transmission spectra of L 98-59 b, c, and d for a clear steam atmosphere (blue) and a hazy steam atmosphere (green). Error bars are shown for observations simulated at $R = 30$. The gaseous species corresponding to the molecular features in each hazy spectrum are shown in the bottom panel at a higher ($R = 1000$) resolution. Here the green line represents the corresponding hazy simulated spectrum in the third panel, while the blue indicates the absorption of H_2O . In this wavelength region, N_2 absorption impacts scale height rather than spectral features, so it is not shown. The number of transits simulated for each planet is set to obtain a 5σ detection of H_2O at $1.38 \mu\text{m}$. For the clear case (blue), this requires three, six, and five transits, while the hazy steam atmosphere requires 9, 20, and 17 transits for L 98-59 b, c, and d, respectively.

4.1. Detecting H_2O with JWST

Although HST may be able to detect the presence of a clear, water-dominated atmosphere on each planet in six transits or less, the addition of Titan-like organic aerosols significantly raises the continuum level between 1.1 and $1.7 \mu\text{m}$, decreasing the sensitivity of the H_2O absorption feature at $1.38 \mu\text{m}$ and tripling the number of transits required for detection (Figure 4). Knowing that the haze particles most strongly absorb at UV/VIS/NIR wavelengths (Tomasko et al. 2008), we revisit this atmospheric scenario with the increased wavelength range of JWST’s NIRISS instrument.

Figure 5 shows model spectra of both a clear and hazy steam atmosphere (the same as shown in Figure 4) with simulated JWST/NIRISS SOSS observations for L 98-59 b, L 98-59 c, and L 98-59 d. The bottom panel accompanies these spectra to show the detailed molecular composition of each hazy steam atmosphere, using L 98-59 d as an example. The blue models show a clear sky spectrum with large H_2O absorption features and data uncertainties calculated for a 5σ detection of the

strongest spectral feature. The green models include a Titan-based organic haze whose refractive indices are derived from Khare et al. (1984), with data uncertainties calculated for a 5σ detection of the same spectral feature.

For a clear steam atmosphere (blue), NIRISS SOSS may be able to rule out a featureless spectrum at 5σ in ≤ 1 transit for all three planets. Although NIRISS’s wavelength range (0.6 – $2.8 \mu\text{m}$) is much more extensive than that of HST/WFC3/G141 (1.1 – $1.7 \mu\text{m}$), H_2O absorption at $1.38 \mu\text{m}$ is still calculated to be the most detectable feature in the spectrum, providing an $\text{S/N} \geq 5$ in exchange for nominal observational time. When considering the presence of a Titan-like haze (green), the number of transits required to detect the same $1.38 \mu\text{m}$ absorption feature with the same confidence level increases to one, two, and two transits for L 98-59 b, c, and d, respectively. This drop in sensitivity is much less dramatic than that seen in HST/WFC3 (Figure 4) and can be attributed to the haze opacity effects in transit that become negligible in the MIR (Robinson et al. 2014). As the haze continuum slope is

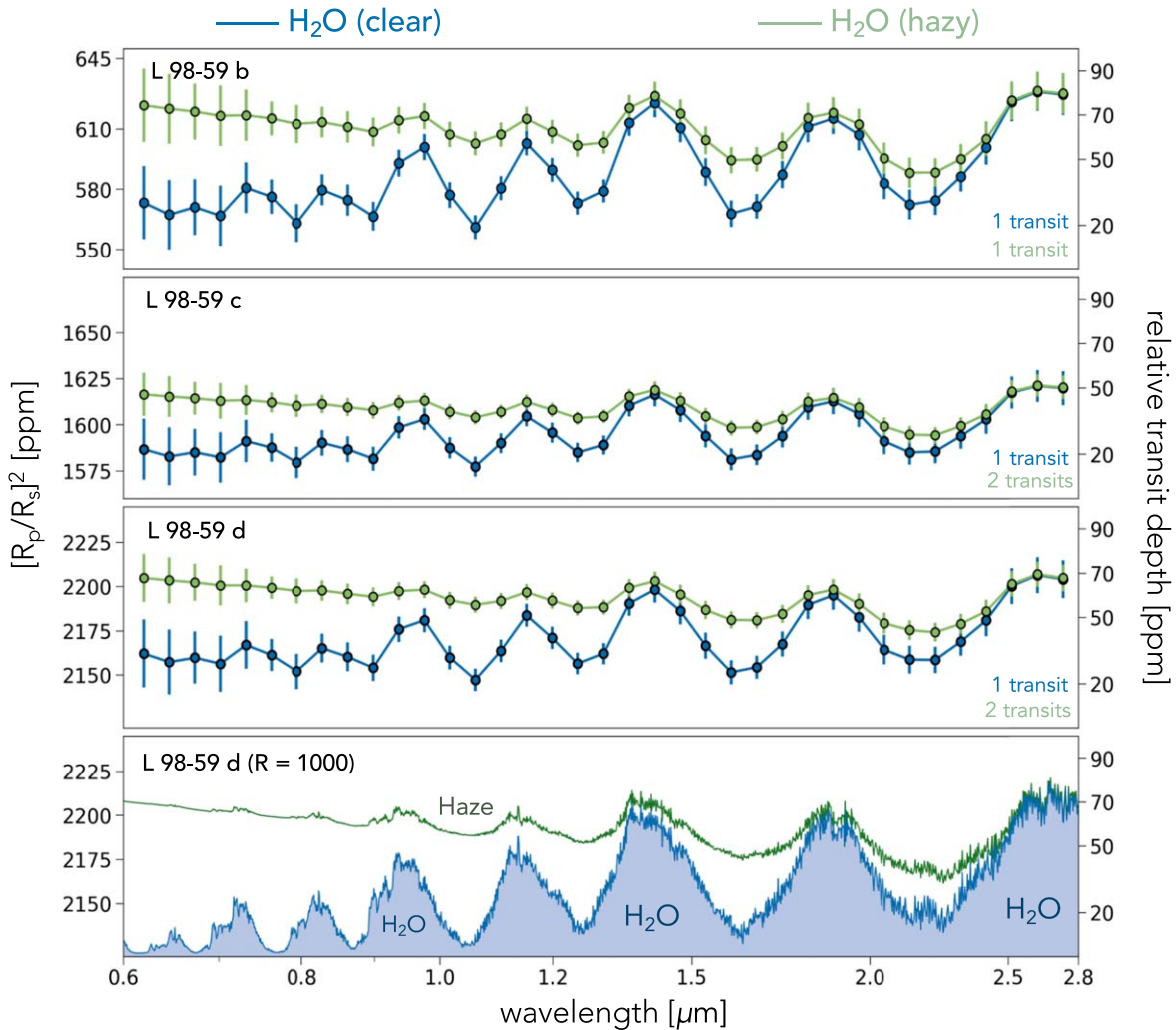


Figure 5. Simulated JWST/NIRISS SOSS transmission spectra of L 98-59 b, c, and d for a clear steam atmosphere (blue) and a hazy steam atmosphere (green). Error bars are shown for observations simulated at $R = 30$. The gaseous species corresponding to the molecular features in each hazy spectrum are shown in the bottom panel at a higher ($R = 1000$) resolution. Here the green line represents the corresponding hazy simulated spectrum in the third panel, while the blue indicates the absorption of H_2O . In this wavelength region, N_2 absorption impacts scale height rather than spectral features, so it is not shown. The number of transits simulated for each planet is set to obtain a 5σ detection of H_2O at $1.38 \mu\text{m}$. For the clear case, this requires one transit for each planet, while the hazy case requires one, two, and two transits for L 98-59 b, c, and d, respectively.

strongly wavelength-dependent, refraction and gas absorption become responsible for distinguishing spectral features beginning around $2.5 \mu\text{m}$, where the magnitude of the transit height variations caused by the haze continuum is no longer as large as the observed gaseous features. Having access to redder NIR wavelengths also allows us to probe for other H_2O absorption features (such as that at $2.6 \mu\text{m}$) that are not diminished by the presence of haze. This multiband detection would increase the certainty level of our observations, which is a critical step in constraining the chemical composition of planetary atmospheres such as these.

4.2. Detecting CO_2 with JWST

One important question to answer is whether or not CO_2 is a dominant gas in the atmospheres of any of these planets. Among the three rocky planets in our solar system with substantial atmospheres, CO_2 dominates two of their atmospheres (Venus and Mars) and is thought to have been a prominent gas in Earth's early atmosphere during the Hadean epoch (Zahnle et al. 2011). Emerging evidence also suggests

that CO_2 was substantially more abundant during the Archean (Catling & Zahnle 2020). This predominance in the solar system suggests that CO_2 atmospheres could be common in other planetary systems as well. Nevertheless, even at the relatively low abundances of today, CO_2 is a critical greenhouse gas that maintains planetary temperatures and generates substantial spectral features.

CO_2 has a strong opacity near $4.3 \mu\text{m}$, allowing for the possibility of achieving a 5σ detection with JWST, as shown by Morley et al. (2017), Lincowski et al. (2018), Krissansen-Totton et al. (2018), Fauchez et al. (2019), Wunderlich et al. (2019), Lustig-Yaeger et al. (2019), and Pidhorodetska et al. (2020) for a variety of modeled atmospheric scenarios when considering the TRAPPIST-1 habitable zone planets. For a post-runaway planet like Venus in our solar system, the detection of CO_2 at $4.3 \mu\text{m}$ will provide a key indicator. CO_2 gas is well mixed in the atmosphere and therefore much less sensitive to thick clouds more likely to be found in the troposphere (Robinson & Catling 2014), and its high mean molecular weight aids in the survival of potential atmospheric escape. In addition, a Venus-like atmosphere is less sensitive to

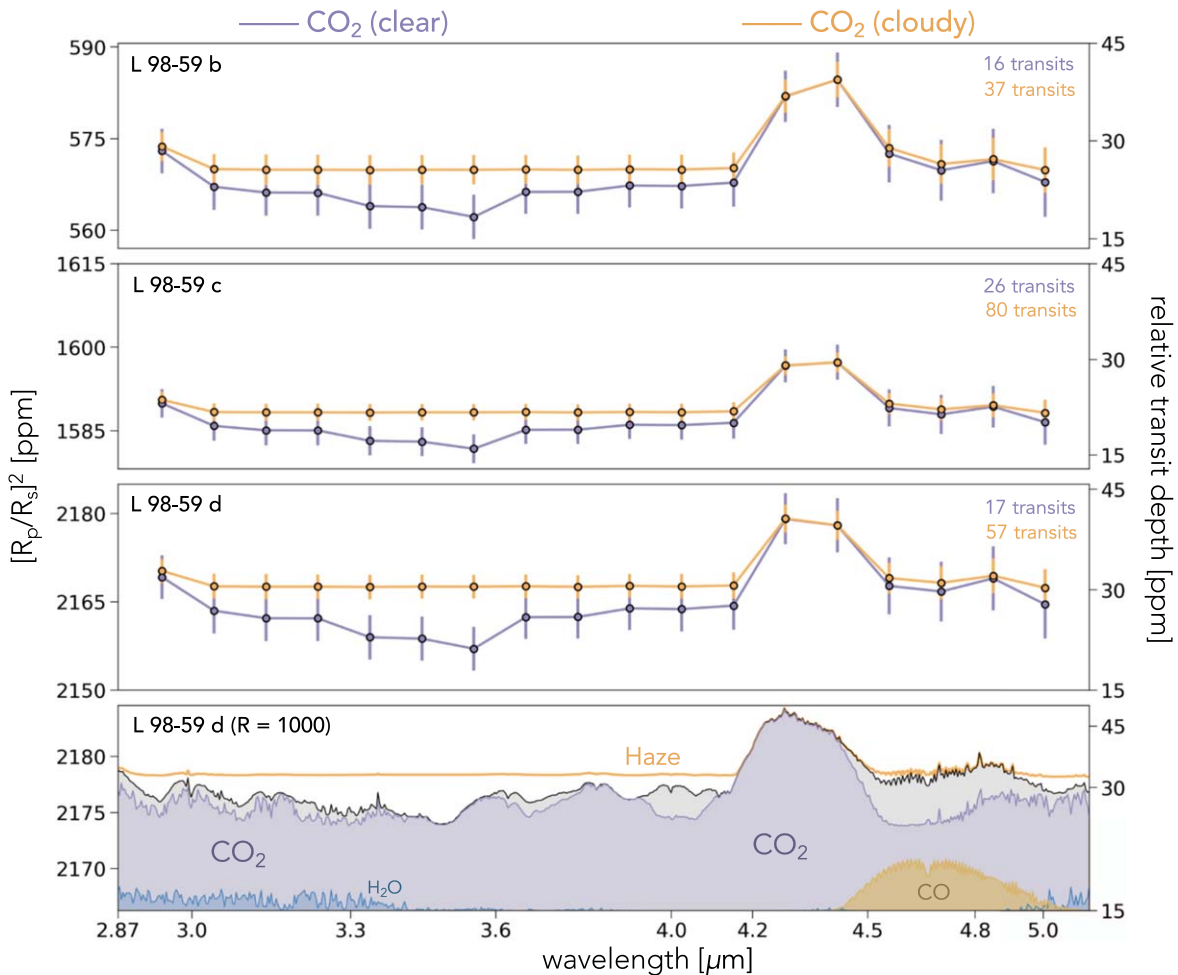


Figure 6. Simulated JWST/NIRSpec G395H transmission spectra of L 98-59 b, c, and d for a clear CO_2 -dominated atmosphere (purple) and a CO_2 -dominated atmosphere that includes Venus-like H_2SO_4 clouds (orange). Error bars are shown for observations simulated at $R = 30$. The bottom panel corresponds to the molecular composition of the cloudy CO_2 atmosphere for L 98-59 d shown at a higher ($R = 1000$) resolution. Here the black line represents the clear simulated spectrum in the third panel, the orange line represents the cloudy simulated spectrum in the third panel, and the gray indicates the sum of all gases present. The absorption of CO_2 is shown in purple, H_2O in blue, and CO in yellow. The number of transits simulated for each planet is set to obtain a 5σ detection of CO_2 at $4.3 \mu\text{m}$. For the clear case, this requires 16, 26, and 17 transits, while the cloudy case requires 37, 80, and 57 transits for L 98-59 b, c, and d, respectively.

changes in temperature due to the low condensation temperature of CO_2 (Morley et al. 2017).

Figure 6 shows model spectra of both clear and cloudy Venus-like atmospheres with simulated JWST/NIRSpec G395H observations for L 98-59 b, L 98-59 c, and L 98-59 d. The bottom panel accompanies these spectra to show the detailed molecular composition of each cloudy atmosphere, using L 98-59 d as an example. The purple models show a clear sky spectrum with large CO_2 absorption features and data uncertainties calculated for a 5σ detection of the strongest spectral feature. The orange models include H_2SO_4 clouds whose refractive indices are derived from Palmer & Williams (1975), with data uncertainties calculated for a 5σ detection of the same spectral feature.

The clear Venus-like atmosphere (purple) shows multiple spectral features (such as at $2.8 \mu\text{m}$) that can be attributed to CO_2 absorption, but the detectability of this atmosphere is dominated by the strength of the $4.3 \mu\text{m}$ CO_2 absorption feature. In this cloud-free scenario, a featureless spectrum could be ruled out at 5σ in 16, 26, and 17 transits for L 98-59 b, c, and d, respectively. This requires considerably fewer transits than the cloudy Venus-like atmosphere (orange), where the H_2SO_4 clouds are located high enough in the atmosphere that a

detection at the same confidence level would involve 37, 80, and 57 transits for L 98-59 b, c, and d, respectively. Contrary to the Titan-like organic haze (Figure 5), the continuum level set by the H_2SO_4 clouds is not wavelength-dependent in the NIRSpec G395H range, causing considerable flattening across the entire spectrum. We note this same effect in the MIRI LRS wavelength range.

4.3. Detecting O_2 with JWST

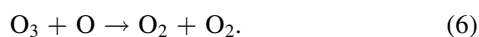
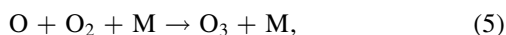
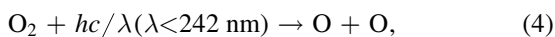
Desiccated O_2 atmospheres have been suggested as one possible outcome of a prolonged runaway greenhouse phase combined with extensive water loss, where all of the oceans in an atmosphere evaporate. Exposed to UV radiation, H_2O breaks into O and H, where the H will then escape. The remaining composition is then dominated by photochemically produced O_2 at least temporarily. Photochemically produced O_2 may then be consumed by a magma ocean. The extent to which O_2 will be left behind in the atmosphere is dependent on a multitude of factors, such as the longevity of the magma ocean, the extent of water loss (and therefore O_2 buildup), the ameliorating effects of O_2 loss via hydrodynamic escape, and subsequent reactions with reducing volcanic gases over time.

Such an atmospheric composition may be common for planets around M-type stars (Luger & Barnes 2015; Tian & Ida 2015; Schwieterman et al. 2016; Meadows 2017; Meadows et al. 2018b; Lustig-Yaeger et al. 2019). In addition, the molecular weight of O₂ makes it more resistant to hydrodynamic escape than less massive homonuclear molecules such as H₂.

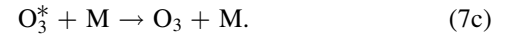
For the TRAPPIST-1 system, Lincowski et al. (2018) showed that for an assumed original water content of 20 Earth oceans (by mass), TRAPPIST-1b, c and d may have lost all their water, while TRAPPIST-1e, f, and g may have lost between three and six Earth oceans. As a result, the atmospheres of these planets may have accumulated the amount of O₂ that would be equivalent to surface pressures between 22 and 5000 bars, if all of the O₂ were to remain in the atmosphere. This mechanism can be limited by oxygen absorption into a magma ocean if temperature conditions are high enough (Wordsworth et al. 2018). However, if the mantle of these planets becomes oxidized, some amount of O₂ could still persist in the atmosphere over geologic timescales. Therefore, it is possible that large amounts of O₂ can still be present in the atmospheres of the TRAPPIST-1 planets (including the innermost), depending on the degree of oxidation of the mantle. This creates a unique opportunity to explore similar cases within the L 98-59 system, providing an avenue for comparative planetology in addition to atmospheric characterization.

Molecular O₂ absorbs through vibrational and rotational transitions at several wavelengths in the VIS at 0.63, 0.69, and 0.76 μm and the NIR at 1.27 μm. In addition, O₂-O₂ CIA produces broad spectral features distinct from individual O₂ absorption features at UV, VIS, and NIR wavelengths. Two O₂-O₂ CIA features are present in the HST/WFC3 wavelength range at 1.06 and 1.27 μm. Although the sensitivity of HST/WFC3 is not strong enough to detect these features on terrestrial planets, JWST's NIRISS could be sensitive enough to probe for these gases. Schwieterman et al. (2016) proposed that these two CIA features could be used in transmission spectroscopy to identify abiotically produced desiccated and dense O₂ atmospheres, building on early work by Misra et al. (2014) that proposed the use of NIR O₂-O₂ CIA features as a method for measuring minimum atmospheric pressure. Lustig-Yaeger et al. (2019) studied this possibility for the TRAPPIST-1 system assuming between 10 and 100 bars of O₂ in the atmospheres of the planets and showed that JWST can detect these O₂-O₂ CIA features at 5σ in just a few transits. In addition, Fauchez et al. (2021) demonstrated that O₂ in low-pressure atmospheres can be detected with MIRI using O₂-X CIA (X can be any gas) at 6.4 μm, assuming no confounding impacts of large H₂O abundances.

When modeling a post-runaway desiccated planet that is rich in abiotic O₂, we expect to see O₃ formation from the photochemical processing of this O₂. The formation and abundance of ozone in a planetary atmosphere will be strongly coupled to its temperature structure. To first order, the formation and destruction in Earth's atmosphere is controlled by the Chapman reaction scheme (Chapman 1930). We write this series of reactions below:



Only one of these reactions (Equation (5)) produces ozone. The rate constant of Equation (5) in the low-pressure limit, which is practically the case throughout the atmosphere, is given as $K_{(5)} = 6.1 \times 10^{-34} (298/T)^{2.4} \text{ cm}^6 \text{ molecules}^{-2} \text{ s}^{-1}$ (Burkholder et al. 2019). This rate constant is geometrically inversely proportional to the temperature of the atmosphere in which the reaction is occurring. This is because the reaction is really a set of three tightly coupled reactions:



Here O₃^{*} is not a distinct species but rather an excited state of O₂ and O in a collisional but unbound state. Without an inert collision to carry away excess energy, the O₃ decays into O₂ (O₃^{*} → O₂ + O). The lifetime of this state is strongly inversely related to temperature, as higher temperatures mean O₂ and O are in proximity for a shorter amount of time and there is less opportunity for M to take away the excess energy. Therefore, we would strongly anticipate that hot planetary atmospheres (T > 300 K) would suppress ozone formation relative to cooler atmospheres. Note that this simplified description does not consider additional catalytic pathways to ozone destruction (e.g., Cl, NO_x, Br, etc.) or atmospheric transport. However, consideration of these pathways would lead to even lower estimates for O₃ prevalence.

Each of the planets in the L 98-59 system has high equilibrium temperatures, though the temperature structures of their atmospheres are unknown and will depend on the presence or absence of stratospheric absorbers and line cooling by molecular species other than O₂. We bound this problem by using Atmos (Arney et al. 2016) to model ozone production in 1 and 10 bar O₂-dominated atmosphere scenarios for both an isothermal temperature of 200 K and an isothermal temperature equal to the equilibrium temperature of the planet (b = 558 K, c = 473 K, d = 374 K). This approach is similar to that previously employed by Fauchez et al. (2021) when estimating the possible range of scale heights relevant to transmission spectroscopy in O₂-dominated atmospheres, except that we also model O₃ photochemistry. The O₃ outputs from the Atmos model are detailed in Figure 7.

Figure 8 shows model transmission spectra representing a variation of four potential O₂ atmospheres for L 98-59 b, c, and d with NIRISS SOSS. The left column shows spectra for 200 K at 1 (yellow) and 10 (orange) bars, while the right column shows spectra for each planet's equilibrium temperature at 1 (red) and 10 (burgundy) bars. The bottom panel accompanies these spectra to show the detailed molecular composition of each 10 bar atmosphere for L 98-59 d.

We find that if the L 98-59 planets possess stratospheric temperatures that are significantly warmer than Earth's (~200–270 K), ozone formation will be suppressed even if their atmospheres are completely dominated by (abiotic) oxygen. At their native equilibrium temperatures (Figure 8 right column), the 1.27 μm O₂ absorption band could be detected at 5σ with 16, 20, and 12 transits (1 bar) and three, six, and seven transits (10 bars) for L 98-59 b, c, and d, respectively. However, at a cooler equilibrium temperature of 200 K (Figure 8, left column), ozone formation increases. In this scenario, the direct detection of O₃ absorption could be another key indicator of a desiccated atmosphere, but we find that the decrease in scale height with temperature renders the

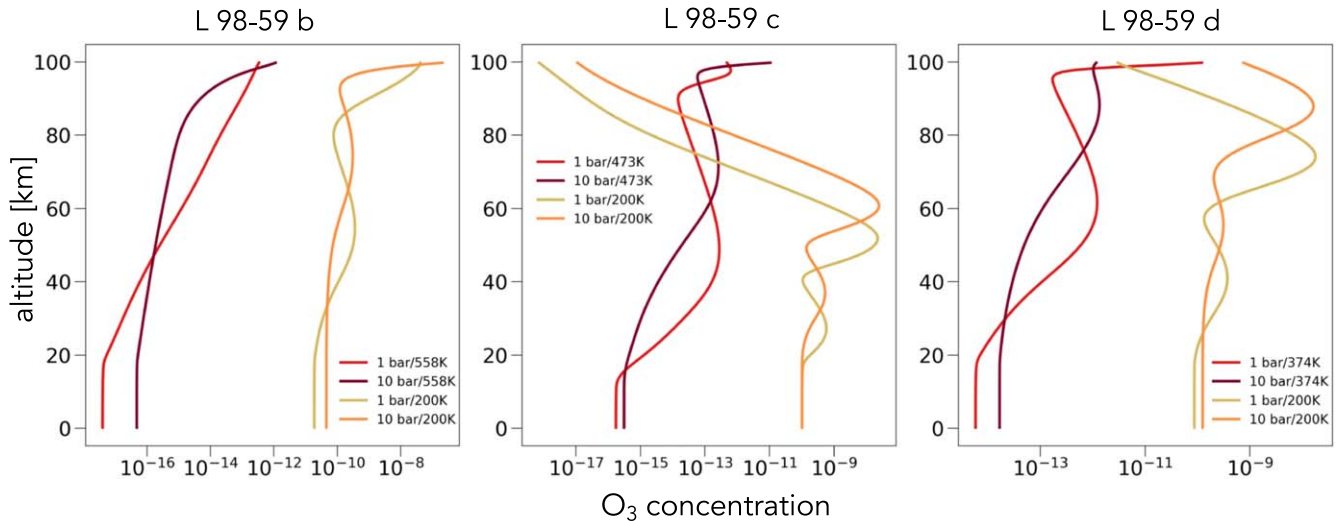


Figure 7. The O_3 concentrations for each modeled O_2/O_3 atmosphere as a function of altitude [km]. These outputs are obtained from the Atmos model.

various O_3 features from 2 to 3 μm undetectable, requiring hundreds of transits for a 5σ detection. The strength of O_2 absorption at 1.27 μm is also significantly diminished, as the transit depth of the feature drops to 10 ppm or less (Figure 8, left column) compared to 20 ppm or less (Figure 8, right column). At 200 K, detection would require 55, 57, and 31 transits (1 bar) and 28, 57, and 31 transits (10 bars) for L 98-59 b, c, and d, respectively. In summary, at low temperatures, ozone formation is more efficient (see bottom left panel of Figure 8), but small scale heights impede ozone detectability. In contrast, at high temperatures, the formation of ozone is suppressed, but this is more than compensated for by increased scale height.

Beyond the wavelength range of NIRSpec, transit observations with MIRI LRS would allow us to search for O_2/O_3 absorption features between 5 and 12 μm . Figure 9 shows model spectra of the same atmospheres in Figure 8 for L 98-59 b, c, and d with MIRI LRS.

For all planets, the broad O_2-O_2 CIA band centered at 6.4 μm becomes increasingly detectable as atmospheric temperatures and pressures are raised. At their native equilibrium temperatures (Figure 9, right column), O_2 could be detected at 5σ with 50, 65, and 40 transits (1 bar) and 12, 23, and 24 transits (10 bar) for L 98-59 b, c, and d, respectively. However, at a cooler equilibrium temperature of 200 K (Figure 9; left column), targeting this feature for a 5σ detection would require upward of 100 transits for each planet at both 1 and 10 bar surface pressures. A direct detection of O_3 could help constrain atmospheric conditions if O_2 is rendered undetectable, but we find that the O_3 absorption feature at 9.7 μm is heavily impacted by noise in the infrared and would require ≥ 200 transits for each of the L 98-59 planets at $T_{\text{eq}} = 200$ K. At their native equilibrium temperatures, less ozone is formed, but the increase in scale height may allow for O_3 detection at 9.7 μm in atmospheres with surface pressures of 10 bars or higher, requiring 36, 41, and 32 transits for L 98-59 b, c, and d, respectively. We find that transit observations with NIRISS SOSS are more optimal than MIRI LRS, as they require significantly fewer transits to detect O_2 absorption features.

5. Discussion

In order to prepare for the future observations of the L 98-59 system that will be carried out using HST and JWST, we performed a series of theoretical models to better understand the atmospheres of the planets in the system and predict the outcome of the planned observations. We limited the analysis to focus on transmission spectroscopy with HST using WFC3 and JWST using NIRSpec G395H, NIRISS SOSS, and MIRI LRS. Our sample consisted of all three planets in the system, with the two innermost being almost certainly rocky, while the outermost is likely a mini-Neptune. These simulations varied the equilibrium temperature, cloud coverage, and overall atmospheric composition. However, they did not represent the full spectrum of possible outcomes. The results presented herein result from some optimistic assumptions regarding planetary parameters and therefore represent lower limits on the amount of observing time needed to detect and characterize atmospheres in the L 98-59 system. As a result, observing plans that include fewer transits than reported here may require additional observations to make robust detections on the nature of these worlds. We now address the influence of these assumptions along with further considerations that would broaden our understanding of our conclusions.

5.1. Atmospheric Profiles

Our simulations did not include the use of a general circulation model (GCM). The GCM simulations conducted at the very high irradiances and temperatures expected for the three planets would be extremely challenging in terms of model stability. Koll & Abbot (2016) showed that simulating the temperature structure of hot (up to 10 times Earth's irradiation) and dry rocky exoplanets with a GCM is only relevant if the atmosphere of high mean molecular weight is hot or thin ($p_{\text{surf}} \leq 1$). Thick atmospheres are expected to be more homogeneous due to a more efficient heat transport, smoothing out horizontal variabilities, therefore mitigating the need for a GCM to simulate the atmospheric structure. Also, if the atmosphere is moist, such as in our steam atmosphere scenario, latent heat transport would reduce the day-night temperature gradient compared to dry atmospheres (Leconte et al. 2013). Therefore, the lack of resolving general circulation in our

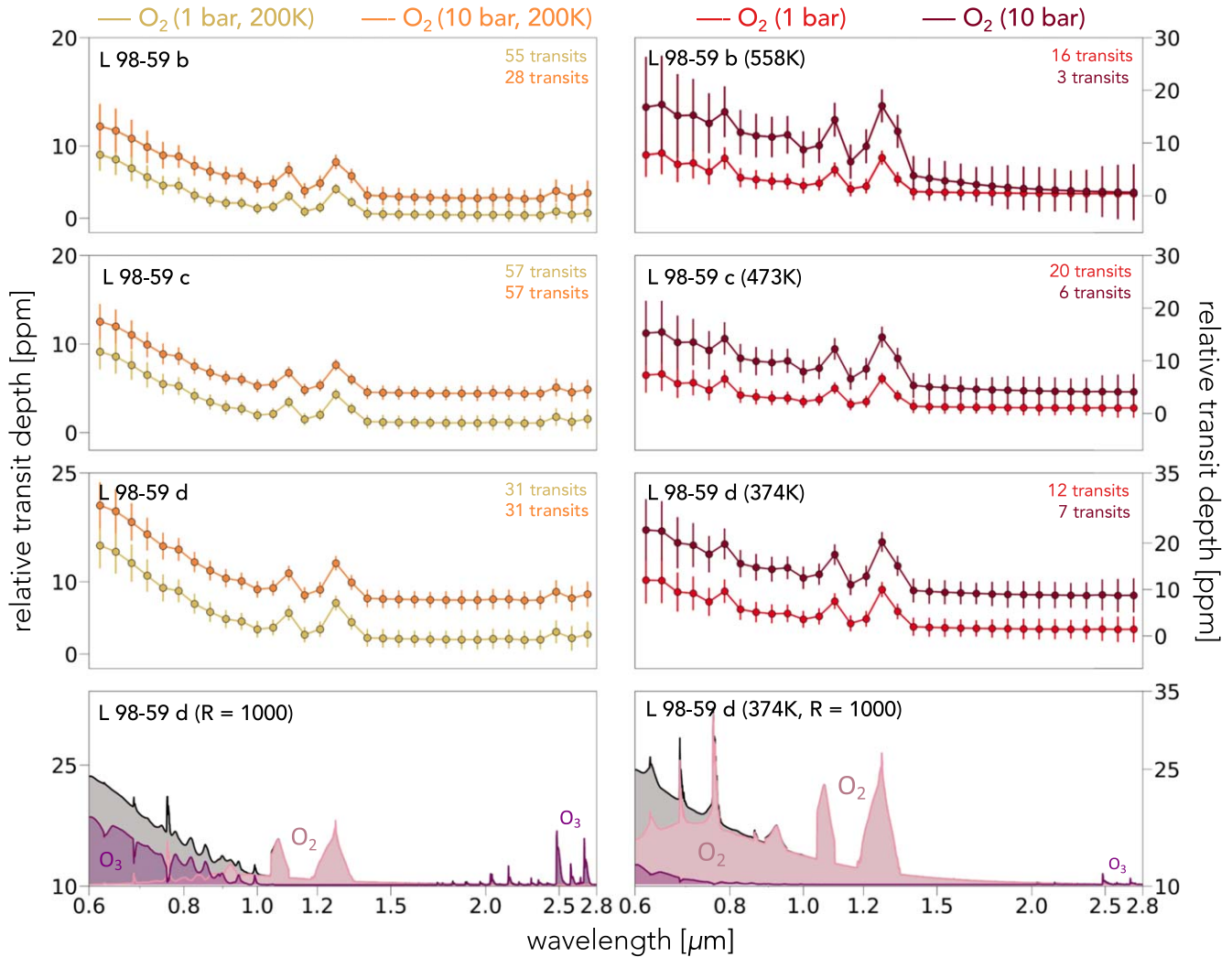


Figure 8. Simulated JWST/NIRISS SOSS transmission spectra of L 98-59 b, c, and d with varying equilibrium temperatures and surface pressures for four possible O₂ atmospheric states. The left column shows 200 K for each planet at 1 (yellow) and 10 (orange) bars, while the right column shows the equilibrium temperature for each planet at 1 (red) and 10 (burgundy) bars. Error bars are shown for observations simulated at $R = 20$. The bottom panel in each column corresponds to the molecular composition of each 10 bar atmosphere for L 98-59 d, which consists entirely of O₂ (pink) and O₃ (purple). The number of transits simulated for each planet is set to obtain a 5σ detection of O₂ at 1.27 μm , with values listed in Table 4.

simulations should not have a significant impact on the temperature and mixing ratio profiles at the terminator.

We did not explicitly compute escape processes. Instead, we calculated thermal escape rates based on the planet’s equilibrium temperature and assumed a Bond albedo of 0.3. A simple calculation such as this one may have over- or underestimated the true rate of escape. Further work would be needed to model escape from this system in detail, but we expect that an H₂ atmosphere would be unstable on short timescales (<100 Myr) under a variety of escape mechanisms, including XUV-driven photoevaporation (Owen & Jackson 2012; Tripathi et al. 2015; Lopez 2017; Murray-Clay et al. 2018), classical Jeans escape, and thermal boil-off (Owen & Wu 2017).

5.2. Emission Spectroscopy

It is important to note that emission spectroscopy could be valuable for highly irradiated planets such as the L 98-59 system. Morley et al. (2017) showed that in the case of TRAPPIST-1b, thermal emission spectra taken in the JWST/MIRI wavelength range are more sensitive to surface pressure

and planetary equilibrium temperature than transmission spectra. Lincowski et al. (2018) also showed that emission spectroscopy can be used in synergy with transmission spectroscopy to improve the discrimination between various atmospheric scenarios. However, in this work, simulations within the JWST/MIRI wavelength range are only considered for O₂-dominated atmospheres to constrain the detectability of O₂-O₂ CIA at 6.4 μm . These modeled atmospheres are isothermal, so they do not have a temperature structure that would allow us to see spectral features in thermal emission.

5.3. Noise and Instrumental Configurations

In this study, we have placed our transmission spectrum simulations in a photon-limited scenario in which the noise would follow a white-noise decay, i.e., proportional to $1/\sqrt{X}$ or $X^{-0.5}$ with X being the number of transits. No noise floor is assumed. We therefore did not consider noise systematics that can be added to the white noise and therefore reduce (in absolute value) the X exponent. Systematics can come from the instrument, for instance, due to intrapixel gain variability (Knutson et al. 2008; Anderson et al. 2011), tracking

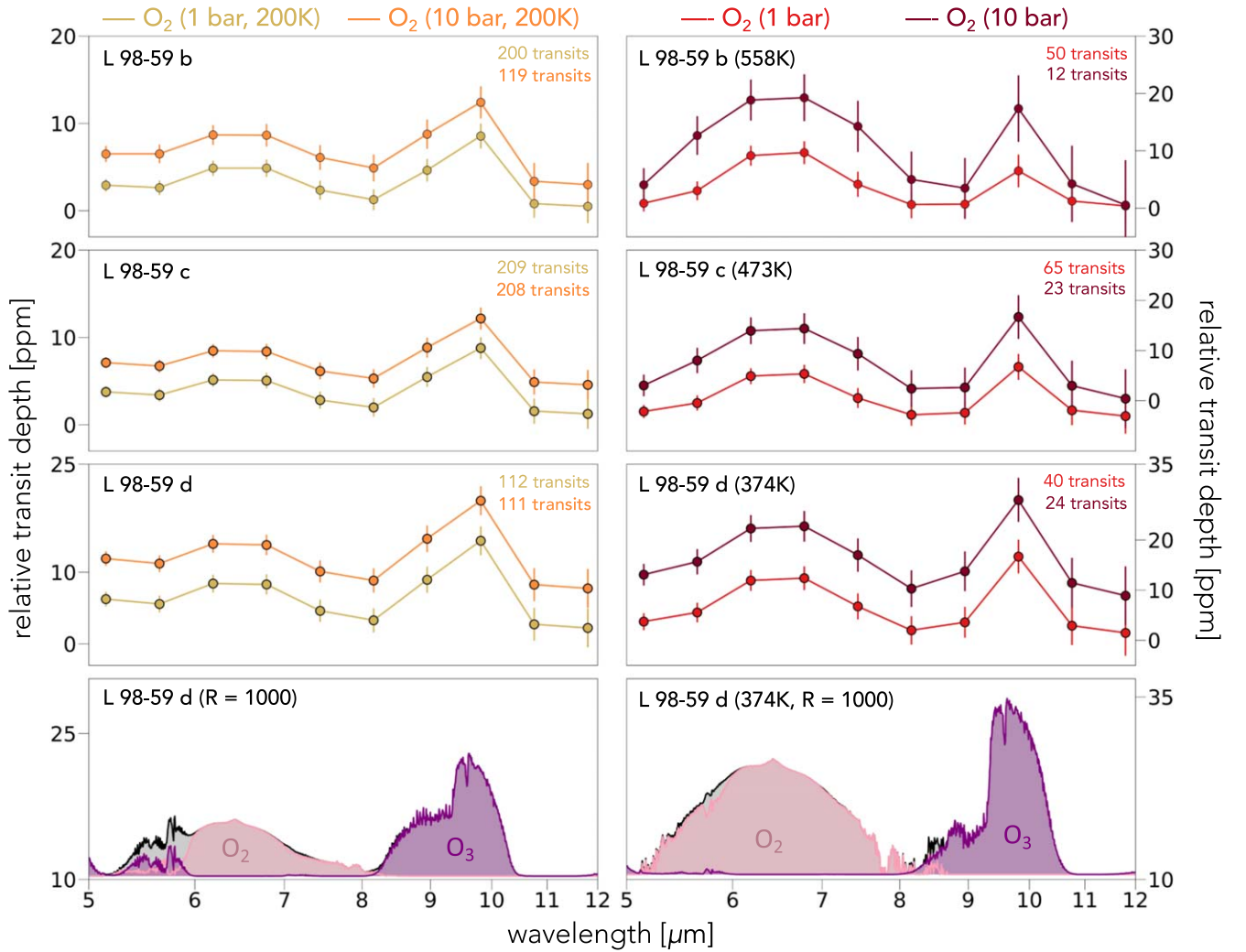


Figure 9. Simulated JWST/MIRI LRS transmission spectra of L 98-59 b, c, and d with varying equilibrium temperatures and surface pressures for four possible O₂ atmospheric states. The left column shows 200 K for each planet at 1 (yellow) and 10 (orange) bars, while the right column shows the equilibrium temperature for each planet at 1 (red) and 10 (burgundy) bars. Error bars are shown for observations simulated at $R = 10$. The bottom panel in each column corresponds to the molecular composition of each 10 bar atmosphere for L 98-59 d, which consists entirely of O₂ (pink) and O₃ (purple). The number of transits simulated for each planet is set to obtain a 5σ detection of O₂ at $6.4 \mu\text{m}$, with values listed in Table 4.

uncertainties, etc. Kreidberg et al. (2014) observations of 15 transits of GJ 1214 with HST/WFC3 have shown a noise decay following a white-noise model. For 55 Cancri e, Tsiaras et al. (2016) reached 20–30 ppm precision over 25 channels in a single transit with HST/WFC3. The fact that a noise floor better than 30 ppm has not been achieved yet with HST/WFC3 does not mean that it is the precision limit of the instrument but rather that not enough transits have been accumulated to actually reach the noise floor. This may be achieved faster with JWST, as its aperture size allows for a larger photon-collecting area. Deming et al. (2009) and Greene et al. (2016) assumed 1σ noise floors for NIRSpec and MIRI LRS of 20 and 50 ppm, respectively, based on the current performance of HST/WFC3. However, this neglects the improvement of the detector stability and data reduction techniques. The JWST’s instrumental noise floors are likely smaller than that (Fauchez et al. 2019; Pidhorodetska et al. 2020) but could not be accurately estimated prior to launch. Therefore, the use of a photon-limited (white-noise) scenario is perhaps adequate for these HST and JWST simulations.

6. Conclusion

Our investigation of the potential to detect and characterize the atmospheres of the L 98-59 planets through transmission spectroscopy indicates that one transit with HST/WFC3 could detect a low mean molecular weight atmosphere on L 98-59 c and d, while one transit with JWST/NIRISS SOSS would allow us to begin distinguishing between a variety of possible atmospheres for each planet in the L 98-59 system. Although the planets are small and likely possess high mean molecular weight atmospheres with relatively low scale heights, we found that many molecular absorption features may be detectable with JWST/NIRSpec G395H and NIRISS SOSS in 2–26 transits.

We find that observations with HST/WFC3 could lead to a 5σ detection of atmospheric spectral features such as CH₄ and H₂O in one transit for H₂-dominated atmospheres on L 98-59 c and d. In addition, HST/WFC3 can detect absorption features in a higher clear mean molecular weight atmosphere such as one dominated by H₂O in six transits or less for L 98-59 b, c, and d. When considering the presence of an organic haze in a steam atmosphere, HST/WFC3 could rule out a featureless spectrum

in 20 transits or less for each planet. However, observations with JWST/NIRISS SOSS could detect the same clear H₂O atmosphere in one transit or less for each planet, and the presence of an organic haze would only increase this to two transits or less for each planet. This boost in detectability is partially due to JWST's increased sensitivity but can also be attributed to NIRSpec's extended wavelength range, where haze opacity becomes negligible in the MIR. With access to redder wavelengths, we can probe for multiple H₂O absorption bands, allowing us to confirm the presence of H₂O with greater confidence while also placing constraints on H₂O abundance via retrieval modeling.

Planets in the VZ that can be spectroscopically characterized are important in the realm of comparative planetology that aims to characterize the conditions of a post-runaway atmosphere. The JWST has a strong ability to detect the presence of an atmosphere dominated by CO₂, as it possesses numerous absorption bands from the NIR through the MIR, such as the 2.0, 2.7, 4.3, and 15 μm bands. This allows for a 5σ detection of a clear Venus-like atmosphere with 16, 26, and 17 transits for L 98-59 b, c, and d, respectively. The addition of Venus-like H₂SO₄ clouds would increase the number of transits required for the same detection to 37, 80, and 57 transits for L 98-59 b, c, and d, respectively. However, a Venus-like planet that has lost its residual hydrogen would not be able to form H₂SO₄ clouds, creating an opportunity for observing stronger features. Although CO₂ makes for a strong indicator of an atmosphere in our simulations, it is a weak discriminant of any specific atmospheric state. Other molecules, such as O₂, O₃, and H₂O, may be detectable with JWST, aiding in the distinction between the suite of atmospheres explored within this work.

Highly irradiated planets such as those of the L 98-59 system could have a desiccated atmospheric composition, such as one that is dominated by O₂, as a result of major ocean loss during an extended runaway greenhouse phase. A desiccated planet that is rich in abiotic O₂ would be expected to form O₃ from the photochemical processing of O₂, meaning that the direct detection of O₃ absorption could be another key indicator of this planetary state. This reaction is temperature-dependent, where hot planetary atmospheres ($T > 300$ K) significantly suppress O₃ formation. In the JWST/NIRISS SOSS (0.6–2.8 μm) and MIRI LRS wavelength ranges (5.0–12.0 μm), the O₂–O₂ CIA band at 1.27 μm provides the strongest S/N compared to all other O₂ bands, allowing for a 5σ detection with 20 transits or less (1 bar) and seven transits or less (10 bars) for all three planets. However, when considering planetary equilibrium temperatures of 200 K, the reduced scale height of the absorption features increases the number of transits required for detection to 55, 57, and 31 (1 bar) and 28, 57, and 31 (10 bars) for L 98-59 b, c, and d, respectively. At these lower temperatures, we see an increase in O₃ formation, but the O₃ absorption features between 2 and 5 μm and at 9.7 μm are too weak to allow for a confident detection. The effects of varying atmospheric temperature between O₂ atmospheres show that it is important to consider a realistic temperature profile for these cases. While we do not expect the detectability to improve significantly when using a calculated temperature profile, we note that these results should be carefully considered. As MIRI LRS calls for significantly more transits to make a confident detection of O₂, we find that NIRSpec and NIRISS are JWST's optimal instruments to

conduct transmission spectroscopy measurements of the L 98-59 planets. We also note that the detection of H₂O in the atmospheres of the L 98-59 planets may help to constrain evolutionary scenarios. High-O₂ atmospheres for planets that exited the pre-main sequence with their atmospheres and interiors completely desiccated, however, will have no water to detect, making water in an O₂-dominated atmosphere a potentially detectable discriminant of incomplete desiccation or outgassing from the planetary interior (Lustig-Yaeger et al. 2019).

D.P. and E.W.S. acknowledge support from the NASA Astrobiology Institute's Alternative Earths team funded under cooperative agreement No. NNA15BB03A and the Virtual Planetary Laboratory, which is a member of the NASA Nexus for Exoplanet System Science and funded via NASA Astrobiology Program grant No. 80NSSC18K0829. This work was also supported by the NASA Interdisciplinary Consortia for Astrobiology Research (ICAR) Program. S.E.M. acknowledges support from NASA Earth and Space Science Fellowship grant 80NSSC18K1109. E.A.G. thanks the LSSTC Data Science Fellowship Program, which is funded by LSSTC, NSF Cybertraining grant No. 1829740, the Brinson Foundation, and the Moore Foundation; her participation in the program has benefited this work. Goddard affiliates acknowledge support from the GSFC Sellers Exoplanet Environments Collaboration (SEEC), which is supported by NASA's Planetary Science Division's Research Program.

ORCID iDs


Daria Pidhorodetska  <https://orcid.org/0000-0001-9771-7953>

Sarah E. Moran  <https://orcid.org/0000-0002-6721-3284>

Edward W. Schwieterman  <https://orcid.org/0000-0002-2949-2163>


Thomas Barclay  <https://orcid.org/0000-0001-7139-2724>

Thomas J. Fauchez  <https://orcid.org/0000-0002-5967-9631>

Nikole K. Lewis  <https://orcid.org/0000-0002-8507-1304>

Elisa V. Quintana  <https://orcid.org/0000-0003-1309-2904>

Geronimo L. Villanueva  <https://orcid.org/0000-0002-2662-5776>

Shawn D. Domagal-Goldman  <https://orcid.org/0000-0003-0354-9325>

Joshua E. Schlieder  <https://orcid.org/0000-0001-5347-7062>

Emily A. Gilbert  <https://orcid.org/0000-0002-0388-8004>

Stephen R. Kane  <https://orcid.org/0000-0002-7084-0529>

Veselin B. Kostov  <https://orcid.org/0000-0001-9786-1031>

References

- Agol, E., Dorn, C., Grimm, S. L., et al. 2021, *PSJ*, 2, 1
- Agol, E., Steffen, J., Sari, R., & Clarkson, W. 2005, *MNRAS*, 359, 567
- Akeson, R. L., Chen, X., Ciardi, D., et al. 2013, *PASP*, 125, 989
- Anderson, D. R., Smith, A. M. S., Lanotte, A. A., et al. 2011, *MNRAS*, 416, 2108
- Angelo, I., Rowe, J. F., Howell, S. B., et al. 2017, *AJ*, 153, 162
- Anglada-Escudé, G., Amado, P. J., Barnes, J., et al. 2016, *Natur*, 536, 437
- Arney, G., Domagal-Goldman, S. D., Meadows, V. S., et al. 2016, *AsBio*, 16, 873
- Barclay, T., Burke, C. J., Howell, S. B., et al. 2013, *ApJ*, 768, 101
- Barclay, T., Pepper, J., & Quintana, E. V. 2018, *ApJS*, 239, 2
- Batalha, N. E., & Line, M. R. 2017, *AJ*, 153, 151
- Batalha, N. E., Mandell, A., Pontoppidan, K., et al. 2017, *PASP*, 129, 064501
- Batalha, N. M. 2014, *PNAS*, 111, 12647
- Benneke, B., Knutson, H. A., Lothringer, J., et al. 2019a, *NatAs*, 3, 813

- Benneke, B., Wong, I., Piaulet, C., et al. 2019b, *ApJL*, **887**, L14
- Berta-Thompson, Z. K., Irwin, J., Charbonneau, D., et al. 2015, *Natur*, **527**, 204
- Bierson, C. J., & Zhang, X. 2020, *JGRE*, **125**, e06159
- Bolmont, E., Selsis, F., Owen, J. E., et al. 2017, *MNRAS*, **464**, 3728
- Borucki, W. J., Koch, D., Basri, G., et al. 2010, *Sci*, **327**, 977
- Borucki, W. J., Koch, D. G., Basri, G., et al. 2011, *ApJ*, **736**, 19
- Borucki, W. J., Koch, D. G., Batalha, N., et al. 2012, *ApJ*, **745**, 120
- Bouchet, P., García-Marín, M., Lagage, P. O., et al. 2015, *PASP*, **127**, 612
- Bourrier, V., de Wit, J., Bolmont, E., et al. 2017, *AJ*, **154**, 121
- Bryson, S., Kunimoto, M., Kopparapu, R. K., et al. 2020, *AJ*, **161**, 36
- Burdanov, A. Y., Lederer, S. M., Gillon, M., et al. 2019, *MNRAS*, **487**, 1634
- Burke, C. J., Christiansen, J. L., Mullally, F., et al. 2015, *ApJ*, **809**, 8
- Burkholder, J. B., Dibble, T. S., Crouse, J. D., et al. 2019, Chemical Kinetics and Photochemical Data for Use in Atmospheric Studies, Evaluation No. 19, JPL Publication, <http://jpldataeval.jpl.nasa.gov/>
- Catling, D. C., & Zahnle, K. J. 2020, *SciA*, **6**, eaax1420
- Chambers, J. E. 2001, *Icar*, **152**, 205
- Chapman, S. 1930, Mem. Roy. Meteor., **3**, 103
- Chen, J., & Kipping, D. 2016, *ApJ*, **834**, 17
- Cloutier, R., Astudillo-Defru, N., Bonfils, X., et al. 2019, *A&A*, **629**, A111
- Cohen, O., Gloer, A., Garraffo, C., Drake, J. J., & Bell, J. M. 2018, *ApJL*, **856**, L11
- Crossfield, I. J. M., & Kreidberg, L. 2017, *AJ*, **154**, 261
- de Wit, J., Wakeford, H. R., Gillon, M., et al. 2016, *Natur*, **537**, 69
- de Wit, J., Wakeford, H. R., Lewis, N. K., et al. 2018, *NatAs*, **2**, 214
- Delrez, L., Gillon, M., Triaud, A. H. M. J., et al. 2018, *MNRAS*, **475**, 3577
- Deming, D., Seager, S., Winn, J., et al. 2009, *PASP*, **121**, 952
- Diamond-Lowe, H., Berta-Thompson, Z., Charbonneau, D., & Kempton, E. M. R. 2018, *AJ*, **156**, 42
- Dittmann, J. A., Irwin, J. M., Charbonneau, D., et al. 2017, *Natur*, **544**, 333
- Dressing, C. D., & Charbonneau, D. 2015, *ApJ*, **807**, 45
- Dressing, C. D., Charbonneau, D., Dumusque, X., et al. 2015, *ApJ*, **800**, 135
- Ducrot, E., Gillon, M., Delrez, L., et al. 2020, *A&A*, **640**, A112
- Ducrot, E., Sestovic, M., Morris, B. M., et al. 2018, *AJ*, **156**, 218
- Edwards, B., Changeat, Q., Mori, M., et al. 2021, *AJ*, **161**, 44
- Ehrenreich, D., Vidal-Madjar, A., Widemann, T., et al. 2012, *A&A*, **537**, L2
- Faucher, T. J., Turbet, M., Villanueva, G. L., et al. 2019, *ApJ*, **887**, 194
- Faucher, T. J., Villanueva, G. L., Schwietzman, E. W., et al. 2021, *PSJ*, **2**, 2
- Fortney, J. J., Mordasini, C., Nettelmann, N., et al. 2013, *ApJ*, **775**, 80
- France, K., Loyd, R. O. P., Youngblood, A., et al. 2016, *ApJ*, **820**, 89
- Fulton, B. J., Petigura, E. A., Howard, A. W., et al. 2017, *AJ*, **154**, 109
- Gao, P., Thorngren, D. P., Lee, G. K. H., et al. 2020, *NatAs*, **4**, 951
- García Muñoz, A. 2007, *P&SS*, **55**, 1426
- Gaudi, B. S., Christiansen, J. L., & Meyer, M. R. 2020, arXiv:2011.04703
- Gillon, M., Jehin, E., Lederer, S. M., et al. 2016, *Natur*, **533**, 221, EP
- Gillon, M., Triaud, A. H. M. J., Demory, B.-O., et al. 2017, *Natur*, **542**, 456
- Gordon, I., Rothman, L., Hill, C., et al. 2017, *JQSR*, **203**, 3
- Greene, T. P., Line, M. R., Montero, C., et al. 2016, *ApJ*, **817**, 17
- Grimm, S. L., Demory, B.-O., Gillon, M., et al. 2018, *A&A*, **613**, A68
- Hansen, B. M. S., & Murray, N. 2012, *ApJ*, **751**, 158
- Hardegree-Ullman, K. K., Cushing, M. C., Muirhead, P. S., & Christiansen, J. L. 2019, *AJ*, **158**, 75
- Hawley, S. L., Davenport, J. R. A., Kowalski, A. F., et al. 2014, *ApJ*, **797**, 121
- Henry, T. J., Jao, W.-C., Subasavage, J. P., et al. 2006, *AJ*, **132**, 2360
- Henry, L. G., & Greenstein, J. L. 1941, *ApJ*, **93**, 70
- Holman, M. J., & Murray, N. W. 2005, *Sci*, **307**, 1288
- Hörst, S. M., He, C., Lewis, N. K., et al. 2018, *NatAs*, **2**, 303
- Howard, A. W., Marcy, G. W., Bryson, S. T., et al. 2012, *ApJS*, **201**, 15
- Howell, S. B., Sobeck, C., Haas, M., et al. 2014, *PASP*, **126**, 398
- Hsu, D. C., Ford, E. B., & Terrien, R. 2020, *MNRAS*, **498**, 2249
- Jenkins, J. M., Twicken, J. D., McCauliff, S., et al. 2016, *Proc. SPIE*, **9913**, 99133E
- Kane, S. R., Barclay, T., & Gelino, D. M. 2013, *ApJL*, **770**, L20
- Kane, S. R., Ceja, A. Y., Way, M. J., & Quintana, E. V. 2018, *ApJ*, **869**, 46
- Kane, S. R., Kopparapu, R. K., & Domagal-Goldman, S. D. 2014, *ApJL*, **794**, L5
- Kasting, J. F. 1988, *Icar*, **74**, 472
- Kasting, J. F., Liu, S. C., & Donahue, T. M. 1979, *JGRC*, **84**, 3097
- Keller-Rudek, H., Moortgat, G. K., Sander, R., & Sörensen, R. 2013, *ESSD*, **5**, 365
- Kempton, E. M.-R., Lupu, R., Owusu-Asare, A., Slough, P., & Cale, B. 2017, *PASP*, **129**, 044402
- Kendrew, S., Scheithauer, S., Bouchet, P., et al. 2015, *PASP*, **127**, 623
- Khare, B. N., Sagan, C., Arakawa, E. T., et al. 1984, *Icar*, **60**, 127
- Kiraga, M., & Stepien, K. 2007, arXiv:0707.2577
- Knutson, H. A., Benneke, B., Deming, D., & Homeier, D. 2014a, *Natur*, **505**, 66
- Knutson, H. A., Charbonneau, D., Allen, L. E., Burrows, A., & Megeath, S. T. 2008, *ApJ*, **673**, 526
- Knutson, H. A., Dragomir, D., Kreidberg, L., et al. 2014b, *ApJ*, **794**, 155
- Kofman, V., & Villanueva, G. L. 2021, *JQSR*, **270**, 107708
- Koll, D. D. B., & Abbot, D. S. 2016, *ApJ*, **825**, 99
- Kopparapu, R. K., Ramirez, R., Kasting, J. F., et al. 2013, *ApJ*, **765**, 131
- Koskinen, T. T., Aylward, A. D., & Miller, S. 2007, *Natur*, **450**, 845
- Kostov, V. B., Mullally, S. E., Quintana, E. V., et al. 2019a, *AJ*, **157**, 124
- Kostov, V. B., Schlieder, J. E., Barclay, T., et al. 2019b, *AJ*, **158**, 32
- Kreidberg, L., Bean, J. L., Désert, J.-M., et al. 2014, *Natur*, **505**, 69
- Kreidberg, L., Mollière, P., Crossfield, I. J. M., et al. 2020, arXiv:2006.07444
- Krissansen-Totton, J., Garland, R., Irwin, P., & Catling, D. C. 2018, *AJ*, **156**, 114
- Lammer, H., Kasting, J. F., Chassefière, E., et al. 2008, *SSRv*, **139**, 399
- Lebonnois, S., & Schubert, G. 2017, *NatGe*, **10**, 473
- Lecavelier Des Etangs, A. 2007, *A&A*, **461**, 1185
- Leconte, J., Forget, F., Charnay, B., et al. 2013, *A&A*, **554**, A69
- Leconte, J., Forget, F., Charnay, B., Wordsworth, R., & Pottier, A. 2013a, *Natur*, **504**, 268
- Leconte, J., Forget, F., Charnay, B., et al. 2013b, *A&A*, **554**, A69
- Libby-Roberts, J. E., Berta-Thompson, Z. K., Désert, J.-M., et al. 2020, *AJ*, **159**, 57
- Lincowski, A. P., Meadows, V. S., Crisp, D., et al. 2018, *ApJ*, **867**, 76
- Lissauer, J. J., Ragozzine, D., Fabrycky, D. C., et al. 2011, *ApJS*, **197**, 8
- Lopez, E. D. 2017, *MNRAS*, **472**, 245
- Lopez, E. D., & Fortney, J. J. 2014, *ApJ*, **792**, 1
- Loyd, R. O. P., France, K., Youngblood, A., et al. 2016, *ApJ*, **824**, 102
- Luger, R., & Barnes, R. 2015, *AsBio*, **15**, 119
- Luger, R., Sestovic, M., Kruse, E., et al. 2017, *NatAs*, **1**, 0129
- Lustig-Yaeger, J., Meadows, V. S., & Lincowski, A. P. 2019, *AJ*, **158**, 27
- Marcq, E., Salvador, A., Massol, H., & Davaille, A. 2017, *JGRE*, **122**, 1539
- Massie, S. T., & Hergiv, M. 2013, *JQSR*, **130**, 373
- Meadows, V. S. 2017, *AsBio*, **17**, 1022
- Meadows, V. S., Arney, G. N., Schwietzman, E. W., et al. 2018a, *AsBio*, **18**, 133
- Meadows, V. S., Reinhard, C. T., Arney, G. N., et al. 2018b, *AsBio*, **18**, 630
- Mikal-Evans, T., Crossfield, I. J. M., Benneke, B., et al. 2021, *AJ*, **161**, 18
- Misra, A., Meadows, V., Claire, M., & Crisp, D. 2014, *AsBio*, **14**, 67
- Moran, S. E., Hörst, S. M., Batalha, N. E., Lewis, N. K., & Wakeford, H. R. 2018, *AJ*, **156**, 252
- Moran, S. E., Hörst, S. M., Vuitton, V., et al. 2020, *PSJ*, **1**, 17
- Mordasini, C., Alibert, Y., Georgy, C., et al. 2012, *A&A*, **547**, A112
- Morley, C. V., Fortney, J. J., Kempton, E. M.-R., et al. 2013, *ApJ*, **775**, 33
- Morley, C. V., Fortney, J. J., Marley, M. S., et al. 2015, *ApJ*, **815**, 110
- Morley, C. V., Kreidberg, L., Rustamkulov, Z., Robinson, T., & Fortney, J. J. 2017, *ApJ*, **850**, 121
- Muirhead, P. S., Mann, A. W., Vanderburg, A., et al. 2015, *ApJ*, **801**, 18
- Mulders, G. D., Pascucci, I., & Apai, D. 2015, *ApJ*, **798**, 112
- Murray-Clay, R., Owen, J., & McCann, J. 2018, AGUFM, 2018, P44A–01
- Ostberg, C., & Kane, S. R. 2019, *AJ*, **158**, 195
- Owen, J. E. 2019, *AREPS*, **47**, 67
- Owen, J. E., & Jackson, A. P. 2012, *MNRAS*, **425**, 2931
- Owen, J. E., & Wu, Y. 2017, *ApJ*, **847**, 29
- Palmer, K. F., & Williams, D. 1975, *ApOpt*, **14**, 208
- Parmentier, V., Guillot, T., Fortney, J. J., & Marley, M. S. 2014, *A&A*, **574**, A35
- Pidhorodetska, D., Faucher, T. J., Villanueva, G. L., Domagal-Goldman, S. D., & Kopparapu, R. K. 2020, *ApJL*, **898**, L33
- Ramirez, R. M., & Kaltenegger, L. 2014, *ApJL*, **797**, L25
- Ricker, G. R., Winn, J. N., Vanderspek, R., et al. 2015, *JATIS*, **1**, 014003
- Robinson, T. D., & Catling, D. C. 2014, *NatGe*, **7**, 12
- Robinson, T. D., Maltagliati, L., Marley, M. S., & Fortney, J. J. 2014, *PNAS*, **111**, 9042
- Roettenbacher, R. M., & Kane, S. R. 2017, *ApJ*, **851**, 77
- Rogers, L. A. 2015, *ApJ*, **801**, 41
- Schwietzman, E. W., Meadows, V. S., Domagal-Goldman, S. D., et al. 2016, *ApJL*, **819**, L13
- Schwietzman, E. W., Robinson, T. D., Meadows, V. S., Misra, A., & Domagal-Goldman, S. 2015, *ApJ*, **810**, 57
- Shkolnik, E. L., & Barman, T. S. 2014, *AJ*, **148**, 64
- Sing, D. K., Fortney, J. J., Nikolov, N., et al. 2016, *Natur*, **529**, 59
- Southworth, J., Mancini, L., Madhusudhan, N., et al. 2017, *AJ*, **153**, 191
- Teamy, N. A., Irwin, P. G. J., de Kok, R., et al. 2006, *Icar*, **181**, 243
- Tian, F., & Ida, S. 2015, *NatGe*, **8**, 177

- Tomasko, M. G., Doose, L., Engel, S., et al. 2008, *P&SS*, **56**, 669
- Tripathi, A., Kratter, K. M., Murray-Clay, R. A., & Krumholz, M. R. 2015, *ApJ*, **808**, 173
- Tsiaras, A., Rocchetto, M., Waldmann, I. P., et al. 2016, *ApJ*, **820**, 99
- Tsiaras, A., Waldmann, I. P., Tinetti, G., Tennyson, J., & Yurchenko, S. N. 2019, *NatAs*, **3**, 1086
- Turbet, M., Ehrenreich, D., Lovis, C., Bolmont, E., & Fauchez, T. 2019, *A&A*, **628**, A12
- Untertorn, C. T., Desch, S. J., Hinkel, N. R., & Lorenzo, A. 2018, *NatAs*, **2**, 297
- Vandaele, A. C. 2020, *Composition and Chemistry of the Neutral Atmosphere of Venus* (Oxford: Oxford Univ. Press), 4
- Villanueva, G. L., Smith, M. D., Protopapa, S., Faggi, S., & Mandell, A. M. 2018, *JQSRT*, **217**, 86
- Vuitton, V., Moran, S. E., He, C., et al. 2021, *PSJ*, **2**, 2
- Wakeford, H. R., Lewis, N. K., Fowler, J., et al. 2019a, *AJ*, **157**, 11
- Wakeford, H. R., Wilson, T. J., Stevenson, K. B., & Lewis, N. K. 2019b, *RNAAS*, **3**, 7
- Winters, J. G., Henry, T. J., Lurie, J. C., et al. 2015, *AJ*, **149**, 5
- Wordsworth, R. D., Schaefer, L. K., & Fischer, R. A. 2018, *AJ*, **155**, 195
- Wunderlich, F., Godolt, M., Grenfell, J. L., et al. 2019, *A&A*, **624**, A49
- Yelle, R. V. 2004, *Icar*, **170**, 167
- Youngblood, A., France, K., Loyd, R. O. P., et al. 2016, *ApJ*, **824**, 101
- Zahnle, K., Claire, M., & Catling, D. 2006, *Geobiology*, **4**, 271
- Zahnle, K., Freedman, R. S., & Catling, D. C. 2011, *Icar*, **212**, 493
- Zahnle, K. J., & Catling, D. C. 2017, *ApJ*, **843**, 122